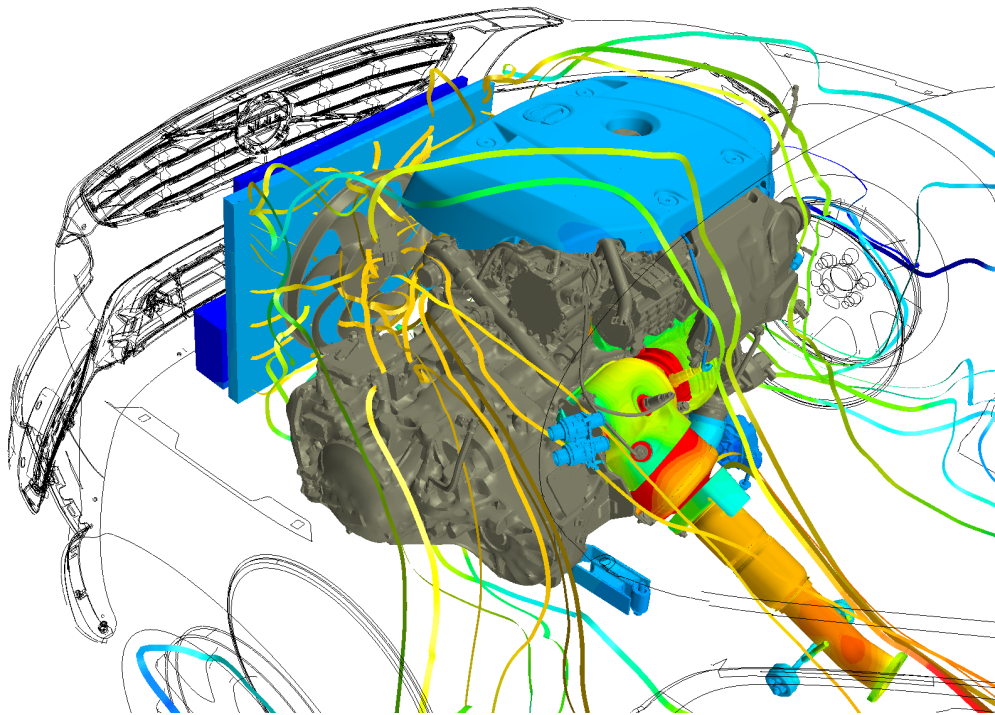




CHALMERS
UNIVERSITY OF TECHNOLOGY



Thermal Analysis of Engine Bay in Star-CCM+

Method Development and Correlation with Experimental Data

Master's thesis in Applied Mechanics

JULIUS LIDAR

MASTER'S THESIS 2018:06

Thermal Analysis of Engine Bay in Star-CCM+

Method Development and Correlation with Experimental Data

JULIUS LIDAR



CHALMERS
UNIVERSITY OF TECHNOLOGY

Department of Applied Mechanics
Division of Fluid Dynamics
CHALMERS UNIVERSITY OF TECHNOLOGY
Gothenburg, Sweden 2018

Thermal Analysis of Engine Bay in Star-CCM+
Method Development and Correlation with Experimental Data
JULIUS LIDAR

© JULIUS LIDAR, 2018.

Supervisor: Marcus Berggren, Semcon
Examiner: Lars Davidsson, Department of Applied Mechanics

Master's Thesis 2018:NN
Department of Applied Mechanics
Division of Fluid Dynamics
Chalmers University of Technology
SE-412 96 Gothenburg
Telephone +46 31 772 1000

Cover: Engine assembly with temperature contours of selected components and streamlines of the flow.

Typeset in L^AT_EX
Printed by Chalmers Reproservice
Gothenburg, Sweden 2018

Thermal Analysis of Engine Bay in Star-CCM+
Method Development and Correlation with Experimental Data
JULIUS LIDAR
Department of Applied Mechanics
Division of Fluid Dynamics
Chalmers University of Technology

Abstract

The use of computational fluid dynamics have a central role today in the automotive industry, but still a lot of decision making is based on knowledge achieved with prototype testing. With the industry driven towards shorter development cycles, the need of more accurate virtual computational methods grow. When the time available for testing is shortend, more and more of the technical ground for decision making need to be entrusted to simulations.

In this thesis a method is developed and evaluated for investigating the thermal balance in the engine bay of a car with focus on the components in close proximity of the exhaust system. A CFD simulation is setup with a finite volume model of a car in a wind tunnel with a fully resolved engine bay, including the internal exhaust gas flow from the exhaust manifold downstream to the first sections of the exhaust pipe. The solids containing the exhaust gases are also included with volume meshes, along with several other solid components included for temperature correlation.

In the following simulations the fluid flow and heat transfer is calculated using the steady state Reynolds-Averaged Navier-Stokes equations, the SST $k - \omega$ turbulence model and the effect of surface-to-surface radiation included. The method also include dual stream modeling and porous media treatment of the front heat exchangers and modeling of the cooling fan with a moving reference frame.

The results show temperatures for several solid components located slightly further away from the exhaust system within a 12% deviation from the test data. This concludes the overall temperature in the engine bay is well captured. The internal exhaust gas temperatures are shown to be predicted within a margin of 6%. However, with the high temperatures of the exhaust gases, this 6% error means around 50 K difference. This deviation can only partially explain the results for the component closest to the exhaust system, the manifold heat shield, which give an error of as much as 40%. This, along with other significant deviations from the test data closer to the exhaust system indicate these components need to be more thoroughly modeled to achieve a full representation of the thermal balance in the engine bay.

Keywords: CFD, automotive, underhood, engine bay, heat transfer, Surface-to-Surface radiation, Star-CCM+, SST Menter $k - \omega$, polyhedral mesh

Acknowledgements

This thesis was performed at Semcon in collaboration with Volvo Car Corporation with Marcus Berggren from Semcon as a supervisor. First of all I would like to thank him for introducing me to the project idea, giving me the opportunity to perform this work and supporting me with his expertise and experience along the way. Thanks also to Niklas Löfgren and Jerry Sjösten at Volvo Car Corporation for supporting the project and providing me with the all necessary input data for my work.

I would like to thank all the employees of the Semcon Simulation department who have been nothing but overly friendly to me from the very beginning and giving me the best working environment I could have hoped for.

Most importantly I would like to thank my wife Emma. You keep helping me to see things with true clarity with your well placed exhortations and give me all the support I need whenever things get a bit too tough. But for the most part we just keep each other smiling and that is what really makes my day, every day.

I would also like to give a special thanks my son Fridolf who arrived towards what should have been the end of the thesis work. Even though it took much longer than expected to wrap up the simulations and finish the report, the work would have been endless without his special way of highlighting the most important parts of life with an unexpected laugh or a sudden flick with his arm.

Julius Lidar, Gothenburg, January 2018

Contents

List of Figures	xi
List of Tables	xiv
1 Introduction	1
1.1 Background	1
1.2 Project purpose	1
1.3 Limitations	1
1.4 Project goal	2
2 Theory	3
2.1 Processes in a car	3
2.1.1 Exhaust system	3
2.1.2 Cooling system	4
2.2 Softwares	5
2.2.1 Star-CCM+	5
2.2.1.1 Star-CCM+ Vocabulary	5
2.2.2 ANSA	6
2.3 Fluid motion and heat transfer	6
2.3.1 Turbulence modeling	8
2.3.1.1 $k - \varepsilon$ model	9
2.3.1.2 $k - \omega$ model	10
2.3.1.3 Menter SST $k - \omega$ model	11
2.3.2 Heat transfer	13
2.3.2.1 Conduction	13
2.3.2.2 Convection	13
2.3.2.3 Radiation	14
2.4 Finite Volume Method	18
2.4.1 Discretization	18
2.4.1.1 Discretizational schemes	19
2.4.2 Geometry preparation	20
2.4.2.1 Surface Wrap	22
2.4.2.2 Interfaces between boundaries and regions	22
2.4.2.3 Boolean Operators, Imprint and Extract Volume	23
2.4.3 Mesh generation	23
2.4.3.1 Element types	23

2.4.3.2	Meshing in Star-CCM+	25
2.5	Modeling motion	25
2.6	Modeling heat exchangers	26
2.6.1	Porous medium	26
2.6.2	Single stream heat exchanger model	27
2.6.3	Dual stream heat exchanger model	27
2.6.3.1	Heat exchanger topology	29
2.7	Modeling radiation	29
3	Method	31
3.1	Model preparation	31
3.1.1	Sealing the inside of the car	31
3.1.2	Surface wrap of the car and wind tunnel	32
3.1.3	Cooling fan	33
3.1.4	Heat exchangers	34
3.1.5	Components for temperature comparison	35
3.1.6	Internal exhaust flow	37
3.1.7	Meshing	38
3.2	Simulation setup	41
3.2.1	Early simulations	41
3.2.2	Main simulation	41
3.2.3	Internal exhaust gas simulation	44
3.2.3.1	Separate transient simulation	45
3.2.3.2	Steady state co-simulation	46
4	Result and Discussion	47
4.1	Temperature comparison	47
4.1.1	Affecting processes	47
4.1.1.1	Internal exhaust gas flow	47
4.1.1.2	Dual Stream heat exchangers	49
4.1.2	Manifold Heat Shield	49
4.1.3	Engine cover	53
4.1.4	Exhaust pipe and exhaust hangers	54
4.1.5	Powertrain Mount	54
4.1.6	Cam belt cover, vacuum hose and vacuum tank	55
4.1.7	Cabin Heater Hose and Turbo Cooling Hoses	55
4.1.8	Charge Air Hose	58
4.1.9	Lambdasond	58
4.2	Interface creation	59
4.3	Calculation stability	61
4.3.1	Residual fluctuations	61
4.4	Future work	62
4.4.1	Polyhedral vs. hexahedral mesh	62
4.4.2	Deeper study of the manifold heat shield	62
4.4.3	Correction of geometrical flaws	62
4.4.4	Transient load cases	63

Bibliography

63

List of Figures

2.1	Geometries used for deriving radiation relations.	15
2.2	A one dimensional grid with center nodes P , W (west), E (east) and EE (east of east). Faces w , e and ee between the control volumes and grid flux at the faces F_w , F_e and F_{ee}	19
2.3	Possible surface errors and how they are highlighted in Star-CCM+	21
2.4	Different element types available for volume meshing.	24
2.5	Heat exchanger topology required by Star-CCM+ for dual stream modeling.	28
3.1	The inside of the car had to be manually sealed off to be excluded from the simulations.	32
3.2	The MRF zone created around the fan with a small gap to the fan itself and the adjacent fan shroud.	33
3.3	The charge air cooler, radiator and subradiator were modeled as dual stream heat exchangers and the condenser (not visible in the figures) as Single Stream.	34
3.4	The components selected for temperature comparison. Manifold Heat Shield (orange), Cabin Heater Hose (light green), Engine Cover (red), Cam Belt Cover (light blue), Vacuum Hose (brown), Vacuum tank (dark green), Lambdasond (pink), Turbo Cooling Hoses (white), Charge Air Hose (yellow), Exhaust Hangers (black), MUPP Rubber (purple), MUPP Bracket (blue), MUPP Shell (cyan), Exhaust system (grey).	36
3.5	The solid parts surrounding the exhaust gases.	37
3.6	The internal exhaust gas flow. The four pairs of inlets are coloured yellow, the manifold green, catalytic converter red, the flexpipe blue and the exhaust pipe purple.	45
4.1	Overview of the engine. The exhaust system and components for temperature comparison are shown with temperature distribution.	48
4.2	Temperature distributions for selected components in the engine bay. Measure point placements are shown in the figures with dots and numbers.	50
4.3	Temperatures for the measure points at the manifold heat shield, normed by their respective measured temperature.	51
4.4	The effect of radiation was tested with a simple simulation of two flat plates facing each other.	52

4.5	Temperatures for the measure points at the engine cover, normed by their respective measured temperature.	53
4.6	Temperatures for the measure points at the exhaust pipe, exhaust pipe stags, exhaust hangers and powertrain mount, normed by their respective measured temperature.	54
4.7	Temperature distributions for selected components in the engine bay. Measure point placements are shown in the figures with dots and numbers.	56
4.8	Temperatures for the measure points at the cabin heater hose, cam belt cover, vacuum hose and vacuum tank, normed by their respective measured temperature.	57
4.9	Temperatures for the measure points at the lambdasond, turbo cooling inlet hose, turbo cooling outlet hose and charge air hose, normed by their respective measured temperature.	59
4.10	A visualization of the interface at the inside of the Manifold heat shield. Green show interfaced faces, grey are faces not included in the interface.	60

List of Tables

3.1	Target and minimum surface sizes used in the surface wrap and mesh.	33
3.2	Coefficient values for Sutherland’s law for air.	35
3.3	Components for temperature comparison along with the material data used.	36
3.4	The division of parts into regions and their used mesh processes. The Automated Mesh was performed as parts-based mesh operation, while the Solid and HXC meshes were performed with a region-based mesh continua.	38
3.5	Parameter values used for the main fluid automated meshing	38
3.6	Parameter values used for the solids automated meshing	39
3.7	Parameter values used for the heat exchangers automated meshing	39
3.8	Parameter values used for the internal exhaust gas automated meshing. Numbers for the area surrounding the turbine wheel are given in brackets.	40
3.9	Models and physics included at different stages of the simulation process.	41
3.10	Solvers used in the main simulation for the main fluid region and solid regions.	42
3.11	Solvers used in the main simulation for the Radiator, Subradiator and Charge Air Cooler regions.	42
3.12	Boundary conditions used. To protect sensitive data temperatures are normed with the same constant temperature as in the contour plots in Chapter 4.	43
3.13	Parameter values for the view factor calculation and surface to surface radiation	45
3.14	Boundary conditions used for the steady state internal exhaust gas flow co-simulation. The temperature is normed with the same constant temperature as in the contour plots in Chapter 4.	46
4.1	Temperatures for the exhaust gases normed with their respective measured result.	48
4.2	Temperatures of the dual stream heat exchanger coolant outlets along heat transfer rates for the respective heat exchanger. All results are normed with respective test results.	49

4.3	Internal ambient temperatures used for the convective boundary conditions in the cabin heater hose and turbo cooling hoses normed by the measured temperature at the respective measure point along with heat transfer coefficients.	57
4.4	Internal static temperatures for the measure points of the charge air hose, normed with their respective temperature measured in the tests.	58

1

Introduction

The possibilities of computer aided engineering improve by the day with both software development and available hardware components. As a result, industry is moving more and more of their research and development from testing to computer simulations.

1.1 Background

The need for virtual computational methods in the automotive industry has increased due to the requirement of shortened development cycles. This means the number of measurements are reduced. To ensure a correct technical ground for decision making, the virtual computational methods need to be improved with respect to results in absolute numbers, something previously entrusted to tests and measurements.

This master thesis aims to develop a method which describe the thermal balance in the engine bay. Focus will be on modeling the hottest components in a physical manner. They affect their environment through heating by conduction, convection and radiation. Selected components are exhaust manifold, turbocompressor and downstream exhaust. To obtain a physical heat transfer from these components to their environment, the exhaust flow needs to be modeled. Boundary conditions for the method development will be taken from tests and available computations.

1.2 Project purpose

Improve current virtual computational methods in the area of thermal balance in the engine compartment of a car.

1.3 Limitations

1. The work is limited to the author working 20 full weeks.
2. The computational power is limited to what Semcon and Volvo can provide.
3. Simulations will only be performed on the specific architecture of the one vehicle model provided by Volvo.

4. Only steady fluid flow simulation will be considered (but transient heat transfer).

1.4 Project goal

Develop a method in Star-CCM+ with the ability to analyze the temperature in sensitive components in the engine bay. The method should include an entire model of a car with a resolved engine bay including all its components. The results from analyzes according to the method should correlate with data from tests and measurements.

2

Theory

This chapter is focused around the finite volume method with theory of the underlying physics of fluid flow and heat transfer, the discretisation of the governing equations and means of preparing and discretizing the geometry. There is also an explanation of relevant processes in a car and a brief introduction to a couple of useful softwares for this project.

2.1 Processes in a car

The engine bay of a car contains a set of complex and intricate systems working together to drive the car, make the climate inside the car comfortable etcetera. The following sections will give a brief view of the subsystems and processes relevant for this thesis and the specific car at hand only.

2.1.1 Exhaust system

The central system of a car is the engine - in this case a combustion engine - which powers the car's propulsion. Inside the engine, a mixture of fuel and air is combusted, to transform the chemical energy of the fuel into angular momentum that drives the car. The internal processes of the engine itself is beyond the scope of this thesis, but in return, some of the appurtenant processes are central.

The mixture of fuel and air is combusted inside the cylinders of the engine. From there the exhaust gases are let out through the *exhaust manifold*, via the *exhaust-gas turbocharger*, through an exit flange, the *catalytic converter* and finally down the *exhaust pipe*. Since the exhaust gases will reach temperatures in the magnitude of a thousand degrees celsius, the parts surrounding them will be substantially heated.

The exhaust manifold gathers the exhaust flow from the engine cylinders down to one single flow. The manifold in this thesis is double jacketed in the sence that the exhaust gases are led from the cylinders in separate pipes, but there is also a larger shell surrounding all the separate pipes. This is a way of reducing the heat transfer from the manifold to the ambient air, since only a small fraction of the exhaust gases will leak out into the larger container.

In the turbocharger, the high pressure exhaust gas is led through a turbine wheel, encased in a turbine housing. The angular momentum obtained is used to pressurize

the fresh air (charge air) going into the engine. This is done with a compressor mounted on the same shaft as the turbine [1].

In the catalytic converter the exhaust gas are cleaned from nitrogen oxides (NO_x), carbon monoxides and hydro carbons through reactions with noble metals at high temperature. A fiber-like structure is used to obtain a large amount of surface in a small volume of space. At the surface is where the actual reaction with the noble metals takes place. This leaves many small conduits for the exhaust gas to pass through [1].

Several mufflers are located further down the exhaust system. The exhaust pipes serve the purpose of connecting the catalytic converter and the different mufflers with each other and leading the hot exhaust gas to the back of the car and let it out into the ambient air where the hot exhaust gases do no damage to the car. Despite this secondary purpose, the geometry and mounting of the exhaust pipes will affect both the performance and the acoustics of the car [1].

2.1.2 Cooling system

An effective combustion requires a mixture of fuel and air. From the chemical formula for the combustion, an optimal air to fuel weight ratio can be calculated. For gasoline, this ratio is approximately 14.7 : 1 [1]. This means a lot more air than fuel is needed.

To be able to get as much air as possible into the engine cylinders, the air is compressed and cooled. The fresh air (or charge air) for the engine is taken in from the front of the car and led through an air filter. The air is then compressed by the turbocharger and supercharger. Next, the charge air is led to the *charge air cooler* (CAC) at the front of the car. This is an air-to-air heat exchanger where the charge air is cooled by the air entering the engine bay from the front of the car. As the charge air is cooled, naturally the ambient air entering the engine bay is heated. The charge air is led from the charge air cooler to the intake manifold where it is distributed over the cylinders of the engine and enters the combustion chambers.

To provide cold air for the air conditioning inside the car, there is another heat exchanger, the *condenser* (COND), in this case located directly behind the charge air cooler. A high temperature gaseous refrigerant is compressed before entering the condenser. When the refrigerant is cooled by the air flowing through the heat exchanger from the front of the car, the refrigerant is returned to a liquid state. The pressure of the refrigerant is then lowered by a pressure valve and the inside of the car is cooled while the refrigerant is vaporated into gas again and once more compressed before entering the condenser[1].

Besides cooling the charge air, the engine and gear box need to be cooled. This is done with the aid of the *radiator* (RAD), an air-to-fluid heat exchanger located directly behind the condenser. Hot refrigerant enters the heat exchanger at one side and exits at the other side, cooled by the air passing through the heat exchanger from the front of the car and into the engine bay. In this case, the major part of

the refrigerant is taken out at the bottom of the radiator, but a smaller amount is taken out at the top, with a slightly lower coolant temperature, to cool the gear box. Even though it is one closed system, the upper part of the radiator is denoted *subradiator* (SUB) and treated separately in calculations (this is further described in Section 3.1.4).

The relative velocity between the ambient air and the car when moving makes sure air enters the engine bay at the front and flows through the heat exchangers. But to improve the flow through the heat exchangers further and to ensure sufficient air flow when the car is still or moving at slow speed, a *cooling fan* is located directly behind the heat exchangers.

2.2 Softwares

Star-CCM+ was chosen prehand to be the main software in this thesis. Apart from Star-CCM+, ANSA is a well known pre-processing software often used for geometry preparation.

2.2.1 Star-CCM+

Star-CCM+ from CD-Adapco is one of the more renowned softwares for performing computational fluid dynamics (CFD). This thesis is devoted to examining how able Star-CCM+ is in obtaining the sought results. While Star-CCM+ is dedicated to CFD calculations, it has been expanded over the years to be a complete tool. Today it can be used through the whole computational process, from editing CAD files to post processing results. It can handle calculations for solids as well as fluids.

2.2.1.1 Star-CCM+ Vocabulary

The vast majority of work in this thesis is performed with Star-CCM+, so a short introduction to the vocabulary of the software is in order. This vocabulary is for the most part common vocabulary for CFD in general.

A file in Star-CCM+ is called a *simulation*. All the needed data can be specified, the intended calculations performed and the results analyzed within a simulation.

A computational domain in Star-CCM+ is called a *region*. Regions are discretized into grids of finite volumes which enables the actual computations to be performed. The process of discretizing a region is called *meshing*. Each region is completely surrounded by *boundaries*. A boundary common between two regions can be joined with an *interface* allowing mass, momentum and energy to pass between the regions.

A *part* in Star-CCM+ is a geometrical representation of an object. Parts can be altered in different ways and used as input for meshing tools. The result of a meshing process will be located in a region specified in advance. One or several parts can be used as input to one region. *Contacts* can be created for surfaces common between

two parts. These contacts are transformed into interfaces when the parts are meshed into regions.

Field functions can be used in Star-CCM+ to define custom mathematical expressions. Field functions can access and make use of all other available variable data in the simulation.

2.2.2 ANSA

ANSA is a pre-processing tool with plentiful of tools for preparing computational domains from CAD to ready-to-use finite element models. It can be used not only for CFD tasks, but several different disciplines. While the softwares for calculations sometimes have built-in tools for preparing a geometry, like Star-CCM+ for instance, a dedicated pre-processor is often chosen because of its extended set of tools and functions that are able to speed up the process of preparing the CAD geometry.

2.3 Fluid motion and heat transfer

The continuity equation (2.1), Navier-Stokes equation (momentum equation) (2.2) and the energy equation (2.5) describe fluid motion and heat transfer for a Newtonian viscous fluid. The continuity equation

$$\frac{d\rho}{dt} + \rho \frac{\partial v_i}{\partial x_i} = \frac{\partial \rho}{\partial t} + \frac{\partial}{\partial x_i}(\rho v_i) = 0 \quad (2.1)$$

derive from the conservation of mass principle and states that, the rate of change of mass in a fluid element, equals the sum of mass flow in and out of the element. ρ denotes density, v_i velocity, t is the time coordinate and x_i is the spatial coordinate. The Navier-Stokes equation

$$\rho \frac{dv_i}{dt} = \frac{\partial}{\partial t}(\rho v_i) + \frac{\partial}{\partial x_j}(\rho v_i v_j) = -\frac{\partial p}{\partial x_i} + \frac{\partial \tau_{ji}}{\partial x_j} + \rho f_i \quad (2.2)$$

derive from the conservation of momentum principle, along with the constitutive laws for a Newtonian viscous fluid

$$\sigma_{ij} = -p\delta_{ij} + \tau_{ij} \quad (2.3)$$

$$\tau_{ij} = \mu \left(\frac{\partial v_i}{\partial x_j} + \frac{\partial v_j}{\partial x_i} \right) - \delta_{ij} \frac{2}{3} \mu \frac{\partial v_k}{\partial x_k} \quad (2.4)$$

Equation (2.3) and (2.4) assume you can additatively decompose the stresses acting on a fluid element, σ_{ij} , into pressure, p , and viscous stresses, τ_{ij} . ρf_i denote body forces, e.g. bouyancy, and the Kronecker delta, δ_{ij} , assures the last term in equation (2.4) acts only in the normal direction. The Navier-Stokes equation states that, the

rate of change of momentum in a fluid element, equals the sum of forces on the the element.

The energy equation

$$\rho \frac{de}{dt} = \frac{\partial}{\partial t}(\rho e) + \frac{\partial}{\partial x_i}(\rho e v_i) = -p \frac{\partial v_i}{\partial x_i} + \Phi - \frac{\partial q_i}{\partial x_i} \quad (2.5)$$

derive from the conservation of energy principle. Here, e denotes internal energy, Φ irreversible viscous heating and q_i heat flux[7]. The energy equation states that, the rate of change of internal energy in a fluid element, equals the sum of energy added and removed from the element in the form of heat and work.

The constitutive law for the heat flux vector, Fourier's law

$$q_i = -k \frac{\partial T}{\partial x_i} \quad (2.6)$$

is used to relate the heat flux to the temperature gradient. k is a material parameter which denotes thermal conductivity.[13]

The above relations give five equations to solve (the continuity equation, the momentum equation in x-,y- and z-direction and the energy equation) with the velocity in three direction, density, pressure, energy and temperature as unknown variables. Equations of state are needed to reduce the number of variables. Two independent state variables, e.g. ρ and T , are sufficient to describe each state of a fluid, assuming thermodynamic equilibrium (which is valid unless very large velocities are present). In the case of a perfect gas, both the pressure and energy can be expressed as functions of density and temperature through the following relations

$$\begin{aligned} p &= \rho R T \\ e &= c_v T \end{aligned} \quad (2.7)$$

where c_v is the specific heat capacity at constant volume and R is a material parameter called the gas constant[13].

In steady-state CFD the temperature, T , is given from the internal energy, e and the density, ρ , is given from T and p . The pressure, p , is given from the SIMPLE algorithm. Basically, this algorithm approximates the velocity field with the pressure field from the previous iteration (or an initial guess), computes a new pressure field from the velocity field and then updates the velocity field using pressure corrections.

2.3.1 Turbulence modeling

It is computationally expensive to directly solve the Navier-Stokes equation so this is in general only done for simple geometries, when an extremely detailed solution is needed. A widespread method to reduce the computational power needed is to assume incompressibility and average the continuity equation (2.1) and Navier-Stokes equation (2.2) in time into the Reynolds-Averaged Navier-Stokes (RANS) equations

$$\frac{\partial \bar{v}_i}{\partial x_i} = 0 \quad (2.8)$$

$$\rho \frac{\partial \bar{v}_i \bar{v}_j}{\partial x_j} = -\frac{\partial \bar{p}}{\partial x_i} + \frac{\partial}{\partial x_j} \left(\mu \frac{\partial \bar{v}_i}{\partial x_j} - \rho \overline{v'_i v'_j} \right) \quad (2.9)$$

First, the velocity and pressure terms in the two equations are replaced by a decomposition into mean and fluctuation terms

$$\begin{aligned} v_i &= \bar{v}_i + v'_i \\ p &= \bar{p} + p' \end{aligned} \quad (2.10)$$

Then the equation is averaged and simplified using relations for the averaged terms into equations (2.9) and (2.8)[6].

All the terms in equation (2.9) are represented also in the Navier-Stokes equation except the last term, which is called the Reynolds stress. An exact equation for this term can be derived from the Navier-Stokes equation but it would be computationally expensive to solve, due to the six unknowns, $\overline{v'_i v'_j}$ ($\overline{v'_x v'_y} = \overline{v'_y v'_x}$). As a remedy, the Reynolds stresses are often modeled using a turbulence model like the $k - \epsilon$ model or $k - \omega$ model.

Incompressible flow is often assumed for flows with a maximum velocity of less than a third of the speed of sound. In this case, the energy equation can be transformed into a temperature equation with the equations of state ($e = c_v T$). This temperature equation can in turn be averaged in a similar manner as the continuity and momentum equations with respect to both the velocity and the temperature resulting in the following expression

$$\frac{\partial \bar{T}}{\partial t} + \frac{\partial \bar{v}_i \bar{T}}{\partial x_i} = \alpha \frac{\partial^2 \bar{T}}{\partial x_i \partial x_i} - \frac{\partial \overline{v'_i T'}}{\partial x_i} \quad (2.11)$$

where $\alpha = \frac{k}{\rho c_p}$ is the thermal diffusivity – a rate between how well a material conducts and stores energy. c_p is the specific heat capacity at constant pressure.

2.3.1.1 $k - \varepsilon$ model

The $k - \varepsilon$ model is the most widely used turbulence model in CFD[13]. It makes use of the Boussinesq assumption which states that the Reynolds stresses, $\overline{v'_i v'_j}$, can be approximated in a similar way as the viscous stresses by introducing a turbulent viscosity, ν_t [6]. In equation form

$$\overline{v'_i v'_j} = -\nu_t \left(\frac{\partial \bar{v}_i}{\partial x_j} + \frac{\partial \bar{v}_j}{\partial x_i} \right) + \frac{1}{3} \delta_{ij} \overline{v'_k v'_k} = -\nu_t \left(\frac{\partial \bar{v}_i}{\partial x_j} + \frac{\partial \bar{v}_j}{\partial x_i} \right) + \frac{2}{3} \delta_{ij} k \quad (2.12)$$

An expression for the turbulent viscosity is then derived through dimensional analysis from the turbulent length scale, ℓ , and the turbulent velocity scale, ϑ , which in turn are obtained from the turbulent kinetic energy, $k = \frac{1}{2} \overline{v'_i v'_i}$, and the dissipation rate, ε .

$$\nu_t = c_\mu \ell \vartheta = c_\mu k^{1/2} \frac{k^{3/2}}{\varepsilon} = c_\mu \frac{k^2}{\varepsilon} \quad (2.13)$$

This reduce the six unknown Reynolds stresses down to two unknowns, the turbulent kinetic energy, k , and the turbulent dissipation rate, ε . An exact equation for k can be derived, in similarity with the Reynolds stresses but some of the terms still needs to be modeled. The modeled k -equation reads

$$\frac{\partial k}{\partial t} + \underbrace{\bar{v}_j \frac{\partial k}{\partial x_j}}_{C^k} = \underbrace{\nu_t \left(\frac{\partial \bar{v}_i}{\partial x_j} + \frac{\partial \bar{v}_j}{\partial x_i} \right) \frac{\partial \bar{v}_i}{\partial x_j}}_{P^k} + \underbrace{g_i \beta \frac{\nu_t}{\sigma_T} \frac{\partial \bar{T}}{\partial x_i}}_{G^k} - \varepsilon + \underbrace{\frac{\partial}{\partial x_j} \left[\left(\nu + \frac{\nu_t}{\sigma_k} \right) \frac{\partial k}{\partial x_j} \right]}_{D^k} \quad (2.14)$$

Here, the production term, P^k , have been simplified using the Boussinesq assumption

$$P^k = -\overline{v'_i v'_j} \frac{\partial \bar{v}_i}{\partial x_j} = \nu_t \left(\frac{\partial \bar{v}_i}{\partial x_j} + \frac{\partial \bar{v}_j}{\partial x_i} \right) \frac{\partial \bar{v}_i}{\partial x_j} \quad (2.15)$$

The turbulent part of the diffusion term, D_t^k , have been simplified with the aid of the standard gradient hypothesis. First the pressure term is omitted since it is usually negligible. Then the turbulent diffusion is approximated with a turbulent viscosity. In equation form

$$D_t^k = -\frac{\partial}{\partial x_j} \left\{ \overline{v'_j \left(\frac{p'}{\rho} + \frac{1}{2} v'_i v'_i \right)} \right\} \approx -\frac{\partial}{\partial x_j} \left\{ \overline{\frac{1}{2} v'_j v'_i v'_i} \right\} = \frac{\partial}{\partial x_j} \left(\frac{\nu_t}{\sigma_k} \frac{\partial k}{\partial x_j} \right) \quad (2.16)$$

And together with the viscous diffusion, D_ν^k , the modeled diffusion term, D^k reads

$$D^k = D_t^k + D_\nu^k = \frac{\partial}{\partial x_j} \left(\frac{\nu_t}{\sigma_k} \frac{\partial k}{\partial x_j} \right) + \nu \frac{\partial^2 k}{\partial x_j \partial x_j} = \frac{\partial}{\partial x_j} \left[\left(\nu + \frac{\nu_t}{\sigma_k} \right) \frac{\partial k}{\partial x_j} \right] \quad (2.17)$$

The buoyancy term, G^k , have first been rewritten with respect to hydro-static pressure and incompressibility into $-\beta\rho_0(\bar{T} - T_0)g_i$, where β is a physical property given from tabulated data and the subscript 0 denotes constant reference values. Then, after decomposing the velocity and temperature into mean and fluctuating values, the term have been simplified during the derivation of the k -equation into $-g_i\beta\overline{v'_i T'}$. Finally, the buoyance have then been simplified using the Boussinesq assumption

$$G^k = -g_i\beta\overline{v'_i T'} = g_i\beta\alpha_t \frac{\partial \bar{T}}{\partial x_i} = g_i\beta \frac{\nu_t}{\sigma_T} \frac{\partial \bar{T}}{\partial x_i} \quad (2.18)$$

where the turbulent diffusivity is given from

$$\alpha_t = \frac{\nu_t}{\sigma_T} \quad (2.19)$$

in similarity with thermal diffusivity. The turbulent Prandtl number, σ_T , is an empirical constant giving a ratio between how well the turbulence transports momentum compared to thermal energy. It is usually set to a value between 0.7 and 0.9[6].

The modeled ε -equation

$$\frac{\partial \varepsilon}{\partial t} + \bar{v}_j \frac{\partial \varepsilon}{\partial x_j} = \frac{\varepsilon}{k} c_{\varepsilon 1} \nu_t \left(\frac{\partial \bar{v}_i}{\partial x_j} + \frac{\partial \bar{v}_j}{\partial x_i} \right) \frac{\partial \bar{v}_i}{\partial x_j} + c_{\varepsilon 1} g_i \frac{\varepsilon}{k} \frac{\nu_t}{\sigma_\theta} \frac{\partial \bar{\theta}}{\partial x_i} - c_{\varepsilon 2} \frac{\varepsilon^2}{k} + \frac{\partial}{\partial x_j} \left[\left(\nu + \frac{\nu_t}{\sigma_\varepsilon} \right) \frac{\partial \varepsilon}{\partial x_j} \right] \quad (2.20)$$

is obtained in a similar manner. For further details on the derivation of the equations refer to [6].

Several modeling constants are present in the equations. The standard values for these are $c_\mu = 0.09$, $c_{\varepsilon 1} = 1.44$, $c_{\varepsilon 2} = 1.92$, $\sigma_k = 1$, $\sigma_\varepsilon = 1.3$. [6]

2.3.1.2 $k - \omega$ model

An alternative approach is the $k - \omega$ model where ω (specific turbulent dissipation rate) instead of ε (turbulent dissipation rate) is solved for in the second equation. The big advantage with this approach is that ω is known in the viscous sublayer. Here, the equations and coefficients of the model are given without further explanation. For further knowledge refer to [14, 15].

$$\frac{\partial k}{\partial t} + \bar{v}_j \frac{\partial k}{\partial x_j} = \tau_{ij} \frac{\partial v_i}{\partial x_j} - \beta^* \omega k + \frac{\partial}{\partial x_j} \left[\left(\nu + \sigma_{k1} \nu_t \right) \frac{\partial k}{\partial x_j} \right] \quad (2.21)$$

$$\frac{\partial \omega}{\partial t} + \bar{v}_j \frac{\partial \omega}{\partial x_j} = \alpha_1 \frac{\omega}{k} \tau_{ij} \frac{\partial v_i}{\partial x_j} - \beta_1 \omega^2 + \frac{\partial}{\partial x_j} \left[\left(\nu + \sigma_{\omega 1} \nu_t \right) \frac{\partial \omega}{\partial x_j} \right] \quad (2.22)$$

$$\nu_t = \frac{k}{\omega} \quad (2.23)$$

$$\varepsilon = \beta^* \omega k \quad (2.24)$$

$$\sigma_{k1} = 0.5, \sigma_{\omega 1} = 0.5, \beta_1 = 3/40, \beta^* = 0.09, \alpha_1 = 5/9 \quad (2.25)$$

2.3.1.3 Menter SST $k - \omega$ model

The $k - \varepsilon$ model show good qualities for free stream flow, but lack in near-wall treatment unless wall damping functions are used. On the other hand, the $k - \omega$ model show good results all the way down through the boundary layer while the free stream treatment is more complicated [13]. The Menter SST $k - \omega$ model is a combination of the two and makes use of the best parts from both the models. It uses the advantages of the $k - \omega$ model close to walls, but switches to the $k - \varepsilon$ further away from walls. Basically this is done through transforming the $k - \varepsilon$ model into a $k - \omega$ model and adding them together with a blending function included [10].

The equations and coefficients of the Menter SST $k - \omega$ model are stated here with only brief comments. For a more detailed explanation refer to [10][11].

The k and ω equations of the model read

$$\frac{\partial k}{\partial t} + \bar{v}_j \frac{\partial k}{\partial x_j} = P_k - \beta^* \omega k + \frac{\partial}{\partial x_j} \left[(\nu + \sigma_k \nu_t) \frac{\partial k}{\partial x_j} \right] \quad (2.26)$$

$$\frac{\partial \omega}{\partial t} + \bar{v}_j \frac{\partial \omega}{\partial x_j} = \alpha S^2 - \beta \omega^2 + \frac{\partial}{\partial x_j} \left[(\nu + \sigma_\omega \nu_t) \frac{\partial \omega}{\partial x_j} \right] + 2(1 - F_1) \sigma_{\omega 2} \frac{1}{\omega} \frac{\partial k}{\partial x_i} \frac{\partial \omega}{\partial x_i} \quad (2.27)$$

[11] where S is

$$S = \sqrt{2S_{ij}S_{ij}} \quad (2.28)$$

[13] and S_{ij} is the strain-rate tensor according to

$$S_{ij} = \frac{1}{2} \left(\frac{\partial v_i}{\partial x_j} + \frac{\partial v_j}{\partial x_i} \right) \quad (2.29)$$

[6] and the blending function F_1 is given as

$$F_1 = \tanh \left\{ \left\{ \min \left[\max \left(\frac{\sqrt{k}}{\beta^* \omega y}, \frac{500\nu}{y^2 \omega} \right), \frac{4\rho \sigma_{\omega 2} k}{CD_{k\omega} y^2} \right] \right\}^4 \right\} \quad (2.30)$$

$$CD_{k\omega} = \max \left(2\rho\sigma_{\omega 2} \frac{1}{\omega} \frac{\partial k}{\partial x_j} \frac{\partial \omega}{\partial x_j}, 10^{-10} \right) \quad (2.31)$$

[11] where y is the distance to the nearest wall. The blending function F_1 accounts for the blending between the original $k - \varepsilon$ and $k - \omega$ models. A couple of additional enhancements are added to the model along with the blending. To prevent overprediction of turbulence in stagnating flow, the production term is limited with

$$P_k = \min \left[\nu_t \frac{\partial v_i}{\partial x_j} \left(\frac{\partial v_i}{\partial x_j} + \frac{\partial v_j}{\partial x_i} \right), 10\beta^* k\omega \right] \quad (2.32)$$

[11]. To improve the handling of adverse pressure gradients, the turbulent viscosity is given as

$$\nu_t = \frac{a_1 k}{\max(a_1 \omega, SF_2)} \quad (2.33)$$

with $a_1 = 0.31$ and the blending function F_2 given as

$$F_2 = \tanh \left\{ \left[\max \left(2 \frac{\sqrt{k}}{\beta^* \omega y}, \frac{500\nu}{y^2 \omega} \right) \right]^2 \right\} \quad (2.34)$$

All the constants, Φ , are given from the constants Φ_1 and Φ_2 according to

$$\Phi = F_1 \Phi_1 + (1 - F_1) \Phi_2 \quad (2.35)$$

where the Φ_1 constants are given in Equation 2.25 according to the $k - \omega$ model, apart from

$$\sigma_{k1} = 0.85 \quad (2.36)$$

and all the Φ_2 constants are obtained from the standard $k - \varepsilon$ model to

$$\sigma_{k2} = 1.0, \sigma_{\omega 2} = 0.856, \beta_2 = 0.0828, \beta^* = 0.09, \alpha_2 = 0.44 \quad (2.37)$$

Though this model looks complex, for the majority of cases it is only a question of a more complicated coding. When it comes to stability and computational power needed, the SST $k - \omega$ model and the standard $k - \omega$ model should perform similar [10].

2.3.2 Heat transfer

Energy transfer that occur between two systems due to a temperature change is called heat. The net transfer of heat will always occur in direction from the hotter to the colder of the two systems. Heat transfer can occur in three different modes: *conduction*, *convection* and *radiation*.

2.3.2.1 Conduction

Conduction is heat transferred between particles (moleculod or atoms) of a substance. It is more prominent in solids, but occur in fluids and gases as well. Conduction is described mathematically by Fourier's law

$$\dot{Q}_{cond} = kA \frac{dT}{dx} \quad (2.38)$$

where \dot{Q}_{cond} is the heat transfer rate, k is the thermal conductivity (a material parameter), A is the area of the substance and dT/dx is the temperature gradient in the depth direction [3].

2.3.2.2 Convection

Convection is heat transfer from a solid surface to a fluid due to both heat transfer between particles (conduction) and heat transfer through the fluid motion (advection). Larger fluid motion will mean larger convectioal heat transfer. If there is no fluid motion, the heat transfer will occur only through conduction. Convection heat transfer is described by Newton's law of cooling

$$\dot{Q}_{conv} = hA_s(T_s - T_\infty) \quad (2.39)$$

where \dot{Q}_{conv} is the heat transfer rate, h is the heat transfer coefficient (a parameter of the specific flow), A_s is the surface area, T_s is the surface temperature and T_∞ is the temperature in the fluid far away from the surface [3].

A useful relation regarding conduction and convection is the Nusselt number defined as

$$\text{Nu} = \frac{hL_c}{k} \quad (2.40)$$

where h is the convection heat transfer coefficient, L_c is a characteristic length and k is the thermal conductivity. The definition of the Nusselt number can be obtained by taking the ratio between convection and conduction

$$\frac{\dot{q}_{conv}}{\dot{q}_{cond}} = \frac{h\Delta T}{k\Delta T/L} = \frac{hL}{k} = \text{Nu} \quad (2.41)$$

Hence, the Nusselt number give a measure of how effective the convection is in relation to the conduction [3].

Both conduction and convection are taken into account in the fluid flow formulation given in Section 2.3 with the fluid motion and the inclusion of Fourier's law in the energy equation.

2.3.2.3 Radiation

Thermal radiation is the transfer of heat through electromagnetic waves due to temperature. It does not need a participating medium like conduction and convection, but is best transferred through vacuum. In general, thermal radiation is dependent on wavelength, but is often simplified with the assumption of wavelength independency, denoted *grey* thermal radiation. Wavelength dependent radiation goes beyond the scope of this thesis, hence only grey thermal radiation is considered here.

Fundamental properties

The radiation energy emitted per unit time and unit area from a surface is denoted emissive power, E , and is described by the Stefan-Boltzmann law as

$$E = \varepsilon E_b = \varepsilon \sigma T_s^4 \quad (2.42)$$

where E_b is the emissive power from a black body (perfect emitter and absorber) and $\sigma = 5.670 \times 10^{-8} W/m^2 K$ is the Stefan-Boltzmann constant. The surface emissivity, ε , is a material surface parameter. It describes how well the surface emits radiation compared to a black body at a given temperature.

In most cases, radiation is dependent on direction. Intensity, $I_e(\theta, \phi)$, is defined as the rate of radiation energy emitted, $d\dot{Q}_e$, in a certain direction per unit area normal to this direction and per unit solid angle about this direction. In equation form

$$I_e(\theta, \phi) = \frac{d\dot{Q}_e}{dA \cos \theta \cdot d\Omega} = \frac{d\dot{Q}_e}{dA \cos \theta \sin \theta \cdot d\theta d\phi} \quad (2.43)$$

where $dA \cos \theta$ is the projection of the infinite area dA at an angle θ from the surface normal (see Figure 2.1a). ϕ defines the direction transversal to the surface normal. $d\Omega$ is the solid angle. Just as the angle of a circle segment can be defined as the arc length divided by the radius, the solid angle of a cone like segment in a sphere is defined as the area on the sphere surface, dS , divided by the square of the radius, r ,

$$d\Omega = \frac{dS}{r^2} = \sin \theta \cdot d\theta d\phi \quad (2.44)$$

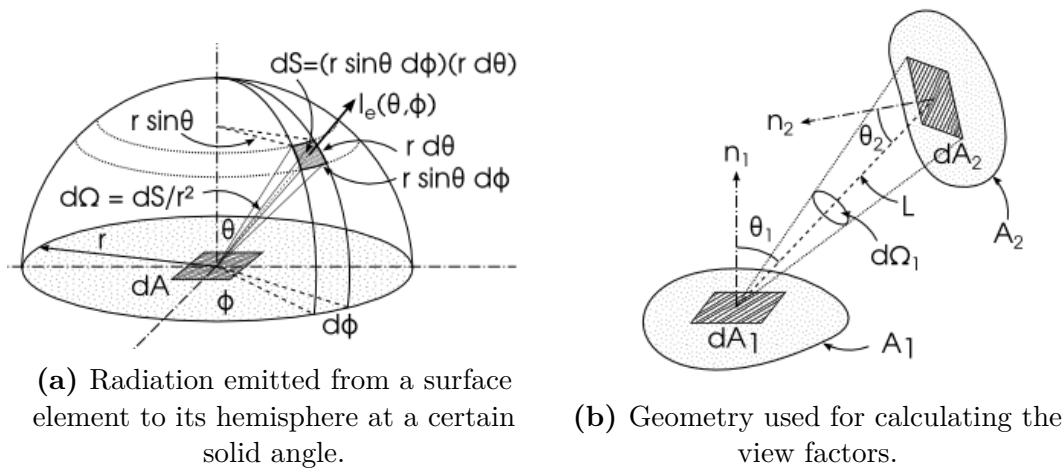


Figure 2.1: Geometries used for deriving radiation relations.

The unit of a solid angle is steradians (sr) so the unit of $I_e(\theta, \phi)$ is W/m^2sr . However, taking the directional variations into account is complicated, so often *diffuse* properties are used with the assumption of radiation being independent of direction [3]. The total emissive power from a surface into its surrounding hemisphere (HS) is given by

$$E = \int_{HS} dE = \int_{HS} \frac{d\dot{Q}_e}{dA} = \int_{\phi=0}^{\phi=2\pi} \int_{\theta=0}^{\theta=\pi/2} I_e(\theta, \phi) \cos \theta \sin \theta d\theta d\phi = \pi I_e \quad (2.45)$$

where I_e is a constant, non-directional emitted intensity and can be defined as

$$I_e = \frac{E}{\pi} = \frac{\varepsilon \sigma T_s^4}{\pi} \quad (2.46)$$

In similarity with diffuse emitted power, diffuse incident radiation, G , onto a surface can be derived to

$$G = \pi I_i \quad (2.47)$$

where I_i is the constant diffuse intensity incident on the surface.

Radiation can also be reflected from a surface. Due to this, it is useful to have an expression for the total rate of radiation leaving a surface. This is called radiosity, J , and is in similarity with diffuse emissive power defined as

$$J = \pi(I_e + I_r) \quad (2.48)$$

where I_r is the diffuse reflected intensity. Diffuse reflectivity assumes radiation is reflected equal in all directions regardless the direction of the incident radiation.

Radiation incident on a surface can be either absorbed, reflected or transmitted. The material parameters describing these capabilities are denoted α (absorptivity), ρ (reflectivity) and τ (transmissivity) respectively. The sum of these three parameters must be unity for a body

$$\alpha + \rho + \tau = 1 \quad (2.49)$$

For opaque bodies, the transmissivity is zero, $\tau = 0$. Also, if gray, diffuse properties are considered the emissivity equals the absorptivity so under these circumstances

$$\varepsilon = \alpha = 1 - \rho \quad (2.50)$$

Radiation in fluids

Radiation is often observed between the surfaces of solids, but a fluid in between two radiating surfaces affect the radiation as well. In many cases though, the effect from a gaseous fluid is relatively small and therefore neglected. For instance clean air mainly transmit radiation without interfering significantly and is often neglected in calculations. However, if large amounts of carbon dioxide, water wapor or particles are present (common with combustion) the radiation may be absorbed or scattered at levels that can not be neglected. In this case the fluid is denoted a participating medium. The levels of the effects of a participating medium are described with the absorption coefficient, κ , and the scattering coefficient, σ_s , and together they are called the extinction coefficient, $\beta = \kappa + \sigma_s$.

Since radiation can be absorbed by a fluid, it must also be emitted. The intensity emitted from a participating fluid medium is given as

$$I_{e,fluid} = \kappa I_{e,b} = \frac{\kappa \sigma T_f^4}{\pi} \quad (2.51)$$

where $I_{e,b}$ is the emitted intensity from a black body.

Radiation Transfer Equation

The governing equation of radiative heat transfer along a ray path is given as

$$\frac{dI(\mathbf{r}, \mathbf{s})}{ds} = \kappa I_b(\mathbf{r}) - \beta I(\mathbf{r}, \mathbf{s}) + \frac{\sigma_s}{4\pi} \int_{4\pi} I_i(\mathbf{s}_i) \Phi(\mathbf{s}_i, \mathbf{s}) d\Omega_i \quad (2.52)$$

where $I(\mathbf{r}, \mathbf{s})$ is the intensity at the position \mathbf{r} in the direction \mathbf{s} , $\kappa I_b(\mathbf{r})$ is the radiation emitted from a participating medium, $\beta I(\mathbf{r}, \mathbf{s})$ is the radiation being extinct by the participating medium, $I_i(\mathbf{s}_i)$ is the incident intensity from all directions \mathbf{s}_i and $\Phi(\mathbf{s}_i, \mathbf{s})$ is the scattering phase function which describe how much of the incident radiation that is redirected into the path \mathbf{s} . The first term in the equation means

rate of change of intensity per unit path length and last term is the in-scattered intensity from all possible directions at location \mathbf{r} . The radiation transfer equation give the total intensity at any point \mathbf{r} in an enclosure which in turn can be used to reveal the radiation heat flux at any boundary.

Radiation between two surfaces are dependent on the orientation of the surfaces (how they face each other). To account for these orientations, view factors are commonly used. A view factor $F_{i \rightarrow j}$ describe the fraction of radiation leaving surface i that strikes surface j directly. If only diffuse properties are considered the denotation is diffuse view factor. The view factors are calculated through a couple of steps. First, the total rate of radiation that leaves a surface dA_1 and strikes a surface dA_2 is

$$\dot{Q}_{dA_1 \rightarrow dA_2} = I_1 dA_1 \cos \theta_1 d\Omega_1 = I_1 dA_1 \cos \theta_1 \frac{dA_2 \cos \theta_2}{L^2} \quad (2.53)$$

where I_1 is the total intensity leaving dA_1 , θ_1 is the angle between the dA_1 surface normal and the line between the surfaces, L , and $d\Omega_1 = dA_2 \cos \theta_2 / L^2$ is the solid angle subtended when viewed from dA_2 (see Figure 2.1b).

The total rate of radiation leaving surface dA_1 is

$$\dot{Q}_{dA_1} = J_1 dA_1 = \pi I_1 dA_1 \quad (2.54)$$

and the view factor is given as the ratio of radiation leaving dA_1 that strikes dA_2 and the total radiation leaving dA_1

$$dF_{dA_1 \rightarrow dA_2} = \frac{\dot{Q}_{dA_1 \rightarrow dA_2}}{\dot{Q}_{dA_1}} = \frac{\cos \theta_1 \cos \theta_2}{\pi L^2} dA_2 \quad (2.55)$$

By integrating the total radiation rate from dA_1 to dA_2 over A_1 and A_2 the radiation rate from the finite surfaces A_1 to A_2 can be calculated through

$$\dot{Q}_{A_1 \rightarrow A_2} = \int_{A_2} \dot{Q}_{A_1 \rightarrow dA_2} = \int_{A_2} \int_{A_1} \frac{I_1 \cos \theta_1 \cos \theta_2}{L^2} dA_1 dA_2 \quad (2.56)$$

From this, the view factor can be extended to the finite surfaces A_1 and A_2

$$F_{A_1 \rightarrow A_2} = \frac{\dot{Q}_{A_1 \rightarrow A_2}}{\dot{Q}_{A_1}} = \frac{1}{A_1} \int_{A_2} \int_{A_1} \frac{\cos \theta_1 \cos \theta_2}{\pi L^2} dA_1 dA_2 \quad (2.57)$$

The theory of view factors can be extended to include the influence of transmissivity and reflectivity which is useful to get a complete representation of the radiation, but this will not be shown here (please refer to [9] for further knowledge on the subject).

Radiation in fluid formulation

In the opposite with conduction and convection, radiation is not included in the fluid formulation and has to be accounted for separately with the use of the radiation transfer equation and view factor calculations. Thermal radiation propagate with the speed of light which makes it quasi-steady. For the most applications, it adapts instantly to changes in the flow. This means no direct coupling with the flow is needed and the radiation can be included parallel with the conduction and convection [13]. Due to this, the influence from radiation will be calculated parallel and added as a source or sink term to the energy equation.

Emissivity

The surface parameter emissivity describe how well a surface emit radiation at a given temperature compared to a black body. The emissivity depend on many things such as surface temperature, wavelength and direction of the emitted radiation, surface material and roughness. As previously stated, taking direction and wavelength into account is complicated, hence gray and diffuse thermal radiation is often used for simplification [3].

The emissivity for pure, smooth metals is close to constant from the radiating surface normal up to about a 50° angle from the surface normal. For larger angles, the emissivity rises to a peak a few degrees from the surface tangent. In reality, surfaces usually have roughness and possibly oxidization, which result in an emissivity closer to diffuse, i.e. an emissivity independent on direction [9, Ch. 3]. So in the case of rough and contaminated metal surfaces, the assumption of diffuse emissivity should be acceptable.

The assumption of grey surface properties can be violated if surfaces in the radiation enclosure have significantly different temperature. This could mean incident radiation at mainly one wavelength and emitted intensity at another wavelength [9].

2.4 Finite Volume Method

The most common approach in computational fluid dynamics is the finite volume method. Its basic principle is to divide the domain into a grid of finite control volumes and discretize the differential governing equations so they can be applied to the grid. In practice, the process of dividing the computational domain into a grid includes first preparing the geometry (i.e. fixing errors and making simplifications) and then meshing the domain into the finite volume grid.

2.4.1 Discretization

From the similarities in the three governing equations a transport equation for a general property ϕ can be formulated as

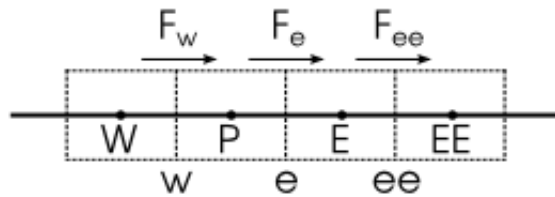


Figure 2.2: A one dimensional grid with center nodes P , W (west), E (east) and EE (east of east). Faces w , e and ee between the control volumes and grid flux at the faces F_w , F_e and F_{ee} .

$$\frac{\partial(\rho\phi_i)}{\partial t} + \frac{\partial}{\partial x_j}(\rho\phi_i u_j) = \frac{\partial}{\partial x_j} \left(\Gamma \frac{\partial \phi_j}{\partial x_i} \right) + S_\phi \quad (2.58)$$

which is the general equation used for discretizing the governing equations in the finite volume method [13]. In words, this equation describes the rate of increase of ϕ of fluid element + the net rate of flow of ϕ out of fluid element = the rate of increase of ϕ due to diffusion + the rate of increase of ϕ due to sources. When integrating equation (2.58) over a three dimensional control volume and applying Gauss's divergence theorem the following equation is obtained

$$\frac{\partial}{\partial t} \left(\int_{CV} \rho\phi dV \right) + \int_A n_j \cdot (\rho\phi u_j) dA = \int_A n_j \cdot \left(\Gamma \frac{\partial \phi}{\partial x_j} \right) dA + \int_{CV} S_\phi dV \quad (2.59)$$

where n denotes the surface normal vector to the surface dA and the product with n and a vector gives the component of that vector in the surface normal direction. Thus, the second term on the left hand side and the first term on the right hand side denote flux of ϕ through the surface A_s through convection and diffusion respectively. By approximating each integral as the flux over the edges of a small control volume, this equation can be applied to a finite volume representation of a 3D geometry.

2.4.1.1 Discretizational schemes

The value of any variable ϕ is stored for the center node of each control volume (element) in the grid, but the fluxes between the control volumes occur at the faces. So the fluxes at the faces are approximated using the center node values of the adjacent cells. The rules of how this approximation is performed is called a discretizational scheme. The fluxes are used to compute new center node values, so in the end, the discretizational scheme relates a new value of a variable ϕ at the center node of a specific control volume, to the old value in the same node and the center node values from one or several adjacent control volumes. Two of the most common discretizational schemes are first order upwind scheme and second order upwind scheme.

The first order upwind scheme simply uses the same property value at the face as the closest center node upwind in the flow. That is

$$\phi_e = \begin{cases} \phi_P & F_e \geq 0 \\ \phi_E & F_e < 0 \end{cases} \quad (2.60)$$

where ϕ_i is the parameter value at face e , node P and node E respectively and F_e is the flux parameter at face e with positive direction from west to east (see Figure 2.2).

The second order upwind scheme use the values from the two closest upstream nodes to approximate the face value

$$\phi_e = \begin{cases} \frac{3}{2}\phi_P - \frac{1}{2}\phi_W & F_e \geq 0 \\ \frac{3}{2}\phi_E - \frac{1}{2}\phi_{EE} & F_e < 0 \end{cases} \quad (2.61)$$

where the subscript EE denote the center node in the 2nd control volume to the east [5].

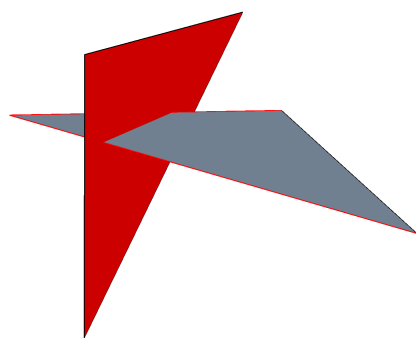
In general, the first order upwind scheme is meritted for being stable however not so accurate while the second order upwind scheme is for the most cases more accurate, but not as stable as the first order upwind scheme. One approach to this is to start using first order upwind scheme to create an approximate solution and then switch to second order to improve the accuracy.

2.4.2 Geometry preparation

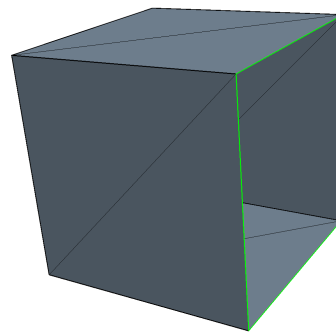
Acquiring the finite volume representation needed to apply the discretized governing equations onto generally requires two steps. First creating a CAD geometry and fixing possible errors in the CAD is referred to as geometry preparation. Second, the prepared geometry needs to be meshed to generate the computational domain made up of finite elements.

Star-CCM+ requires a volume to be closed and manifold in order to allow it to be meshed and later used in simulations. To ensure this, the surface surrounding the volume is not allowed to have any pierced faces, free edges, non-manifold edges or non-manifold vertices. Star-CCM+ offers diagnostic tools to locate and highlight these errors.

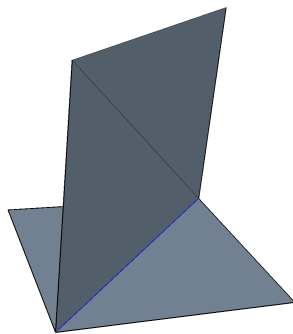
A *pierced face* occurs when a face is intersected by another face, as shown in Figure 2.3a. In Star-CCM+ diagnostics, pierced faces and edges piercing a face are colored red. *Free edges* are only connected to one face (Figure 2.3b). These edges are colored green in the Star-CCM+ diagnostics. The effect of free edges is that the attached surface does not make up a closed volume, but just surfaces without a thickness. *Non-manifold edges* are edges connected to three or more faces (Figure 2.3c). This can be the case for internal surfaces attached to outer surfaces. These should either be deleted or used to split the volume in two, to obtain meshable volumes. A *non-manifold vertex* is one were the vertex itself is the only connection between two faces (Figure 2.3d). Both non-manifold edges and vertices are colored blue in the Star-CCM+ diagnostics.



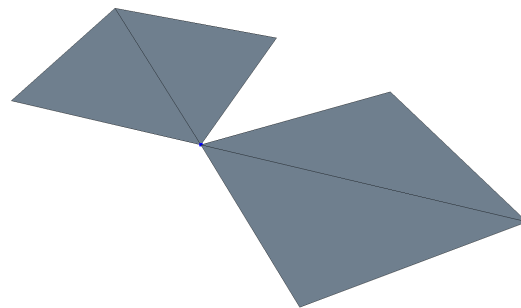
(a) Pierced face



(b) Free edges



(c) Non-manifold edge



(d) Non-manifold vertex

Figure 2.3: Possible surface errors and how they are highlighted in Star-CCM+

All these errors can be corrected within Star-CCM+. The most basic way to do so is within the *Repair surface mode* where one or many faces can be deleted, created, split, moved etcetera. This approach of correcting surface errors may be appropriate when the errors are not too numerous [4].

A more prominent way to correct surface errors is to adjust the original CAD model. This too can be done in Star-CCM+, but also in other pre-processing softwares. This way the larger curved surfaces of the CAD can be adjusted before they are transformed into a mesh with flat smaller surfaces.

2.4.2.1 Surface Wrap

The surface wrap in Star-CCM+ is a useful tool for complex geometries or when the number of surface errors are large. From one or more parts, the surface wrap tries to create a volume with one closed outer surface, by stitching the input surfaces together and closing small gaps. As a result, the input surfaces are not fully maintained, but degraded to achieve the final closed volume. The surface wrapper can be setup to find the inside or outside of a sought volume.

There is an additional tool within the surface wrap called *leak detection*. It is used to make sure that no leaks will occur in the sought volume. It works by trying to trace a path between two user specified points. This way, possible leaks that the surface wrap can not close automatically can be repaired before the actual surface wrap is performed.

The Surface wrapper comes with the option to perform *partial wrapping*. It is possible to choose which of the input parts to preserve with this property activated. The surface wrapper performs the wrap as usual, but afterwards imprints the wrapped surface onto the original surface of the parts specified to be preserved. This way, the surface of chosen parts can be almost fully preserved while still properly connected to its adjacent parts.

2.4.2.2 Interfaces between boundaries and regions

The discretized domains in Star-CCM+ are called regions. A region can for example be one or more solid parts, an entire fluid domain or part of a fluid domain which needs special treatment. To be able to pass any information like mass, momentum and energy from one region to another, Star-CCM+ requires *interfaces* to be specified between the regions. These interfaces are defined at boundaries in close proximity or shared by two regions.

There are a number of different types of interfaces which can be used for different purposes. *Baffle interfaces* are treated like walls with no thickness and can be used to define the surface of regions within the same continuum where no flow is wanted across the interface. *Internal interfaces* connect different regions within the same continuum where flow should be present across the interface. *Contact interface* can be used to define the contact between a fluid and a solid region or two solid regions to allow heat transfer to occur across the interface and the possibility to specify a heat transfer resistance.

There is also a distinction between direct and indirect interfaces. The contact interface is direct, meaning the surfaces of the interface are imprinted onto one another to create a direct contact between the regions. A *mapped contact interface* is indirectly created by mapping one surface onto another. No physical contact between the surfaces occur, but for instance heat can be transferred from one region to the other.

Since the direct interfaces are imprinted, a *conformal mesh* is obtained. This means the mesh is identical on the surfaces of both the regions and the transfer of mass, momentum etcetera can be direct. If the surfaces of the interface are not perfectly matching though, some faces may be left out of the imprint, leaving blank spots on the interface where no transfer will occur. For the indirect interfaces, the faces does not match perfectly. Instead proportional transfer of properties are done to simulate the interface.

There is also the possibility of creating interfaces between entire regions, not only boundaries. For instance, this is used when simulating a dual stream heat exchanger. Each cell of one of the regions is connected to the equivalent cell of the other region, allowing heat to be transferred in each cell in the regions.

2.4.2.3 Boolean Operators, Imprint and Extract Volume

To alter geometry in Star-CCM+ there is the option of using boolean operators. The *unite* tool will merge two or more parts into one, getting rid of any intersections of these parts. The *intersect* tool will do the opposite - keeping only the volume intersected by two or more parts, while deleting the rest. The *subtract* tool is used to remove all the intersecting volume of one or more parts from another part. The *imprint* tool is used to close small gaps between parts by moving the surface of one part to align with the other part surface and deleting any resulting duplicate surfaces. Another useful tool for generating a sought volume is the *extract volume*. It can create one single volume from a void surrounded by several different parts.

2.4.3 Mesh generation

Meshing is the process where the computational domain, originally delimited by smooth CAD surfaces, is transformed into a finite volume representation onto which the discretized governing equations are applied. The meshing is usually made in two steps. First the smooth CAD surface is meshed into a more angular surface made up of small flat triangles, so called surface meshing. In the next step the volume of the computational domain is meshed and incorporated with the meshed surface, called volume meshing.

2.4.3.1 Element types

In the process of volume meshing, a couple different element (or cell) types can be used, namely tetrahedral, hexahedral and polyhedral elements. There are also prism cells, which is basically one of the other element types used in the special purpose

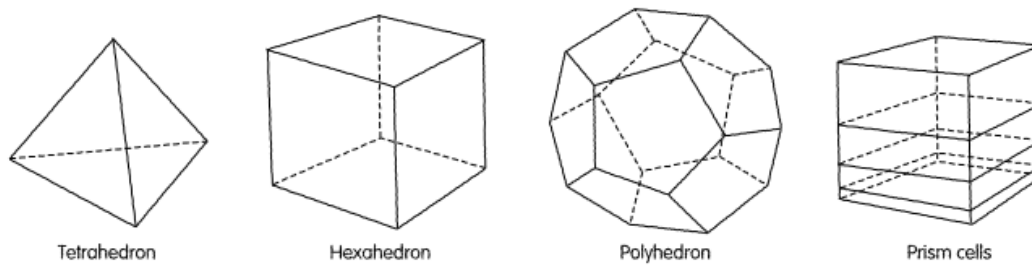


Figure 2.4: Different element types available for volume meshing.

of creating thin cell layers close to surfaces. All these element types are shown in Figure 2.4.

Tetrahedral elements are the most basic cell type made up of four triangular surfaces. Even for complex geometries, a tetrahedral mesh is relatively easy to generate automatically [12] with Delunay triangulation (please refer to literature for details on Delunay triangulations, for example *Finite Element Mesh Generation, Daniel S.H. Lo*). On the downside the tetrahedral elements can not be stretched a lot which mean a large number of elements are needed to achieve accurate results [12]. Also, with only four sides, calculating gradients in certain directions may be difficult with standard approximations [12].

A mesh of *hexahedral elements* is regularly used with polyhedral elements adjacent to surfaces (often hexahedral elements with a cut corner). This kind of mesh can be generated easily and quick for also complex geometries. The mesh is generated from a uniform mesh which is trimmed to match the underlying surface mesh. A smaller number of elements are needed for a hexahedral mesh of defined volume compared to a tetrahedral mesh and the hexahedral elements are better allowed to be skewed. However, the hexahedral mesh, with six faces of each element, is aligned giving three major flow directions. If the flow does not match one of these flow directions, the accuracy of the results may be affected.

Polyhedral elements in average have a larger number of faces than both tetrahedral and hexahedral elements. In Star-CCM+ polyhedral elements have an average of 14 faces [4]. This means more neighbouring cells and a higher probability of gradients being able to be calculated with standard linear shape functions [12]. Also, in Star-CCM+, five times less polyhedral elements are needed for a given volume compared to tetrahedral elements [4]. Polyhedral elements can be generated through a dualization scheme from previously generated tetrahedral mesh. This means that an additional step is needed to generate the polyhedral mesh, while the number of cells are less and the equations can be kept simpler. The polyhedral cells are also said to better handle areas with circualting flow than a hexahedral mesh. A hexahedral element with six faces have three optimal flow directions, while a polyhedral element with twelwe faces have six optimal flow directions [12]. Together, these advantages have proven to give faster computational times, better convergence and less memory usage due to number of cells [12][8]. The downside of polyhedral meshes is the computational power needed for the mesh generation. A polyhedral mesh is gener-

ated by first creating a tetrahedral mesh and then converting it to polyhedrals, so two steps instead of one. Also, the algorithms converting the mesh into polyhedrals require a substantial amount of computing power and memory.

Prism layer cells are thin hexahedral or polyhedral elements used to capture the boundary layer close to surfaces. They can be combined with a hexahedral or polyhedral mesh and it is advised to gradually increase their height to get a smooth transition in cell size to the main grid.

2.4.3.2 Meshing in Star-CCM+

The meshing process in Star-CCM+ is very much automatized. A meshing process is specified with several parameters that control the outcome of the mesh, but the meshing itself is performed in the background by the software.

There are two different approaches when meshing in Star-CCM+. One way is working at part level, called *parts-based meshing*. This way, several operations can be set up that alter the geometry, create contacts and perform the actual mesh. The big advantage with this approach is that a change can easily be made all the way back at CAD-level and all the changes added with operations updated with the push of a button. On the downside, this is the new approach and all functionality is not included this way.

The alternative, old way is to mesh at the region level, called *region-based meshing*. Here all the full functionality of Star-CCM+ is available, but any change in the geometry have to be manually updated. The parameters controlling the outcome of the mesh are similar. In the end, all finite volume meshes are stored in regions, so both the approaches can be used parallel in one simulation.

2.5 Modeling motion

There are several possible ways of modeling the effects of a fan. In Star-CCM+ some examples are fan momentum source model, rotating reference frame and unsteady sliding mesh. The fan momentum source model introduce the effects of the fan by adding source terms to the momentum equation. This offers a calculation effective way to include a fan, but in order to do this, several parameters of the fan performance need to be included, hence, quite good knowledge about the fan is needed. If the needed parameters are well known, the model can produce reasonably good results.

Unsteady sliding mesh is a transient model, meaning that fluctuations in time from the fan will be calculated. The model makes use of the geometry of the fan itself to generate the results, but due the transient calculations, substantially more calculation time is needed.

The rotating reference frame is a middle way. A moving reference frame (MRF) is a region with a rotating and/or translating motion defined relative to the global reference frame of the simulation (lab reference frame). By assigning a local coordinate system and a motion vector (rotating and/or translating) to the MRF zone,

Star-CCM+ can use an actual fan geometry to calculate a constant grid flux. The grid flux is added as a source term in the momentum equation to calculate the mass transfer across faces and hence to take into account how the fan affects its surroundings.

2.6 Modeling heat exchangers

To model a heat exchanger, there is the option to use the actual geometry of the heat exchanger. Due to complex geometries, a simplified model is often used to imitate the physical behaviour of the heat exchanger. Star-CCM+ gives the possibility to simulate the flow resistance through a heat exchanger with *porous medium* and two options for modeling the heat transfer occurring in the heat exchanger, *single stream* and *dual stream*.

2.6.1 Porous medium

Darcy's law describe the pressure loss for a fluid flow through a porous media

$$\frac{dp}{dx_i} = -\frac{\mu}{\kappa}v_i \quad (2.62)$$

where κ is the permeability of the porous media. To better describe the pressure loss for flows with higher velocities, an elaboration of Darcy's law by adding a term for inertial losses was first suggested by Forchheimer [2]. This can be expressed as

$$\frac{dp}{dx_i} = -C_v\mu v_i - C_i \left(\frac{1}{2}\rho|v_i|v_i \right) \quad (2.63)$$

where C_v and C_i are viscous and inertial constants respectively. In this equation, the viscous term will be dominant for small flow velocities while the inertial term will be dominant for large flow velocities.

The pressure drop through a heat exchanger can be simulated by using a porous media instead of including the actual geometry with many thin pipes. The flow resistance through a porous medium in Star-CCM+ is added as a source term in the momentum equation (2.2). This source term reads

$$f_P = -Pv = (P_v + P_i|v|)v \quad (2.64)$$

where P is the porous resistance tensor. P_v and P_i are the viscous and inertial resistance tensors respectively. This equation is a further contraction of Equation 2.63. If the viscous and inertial coefficients are given as C_v and C_i according to Equation 2.63, the coefficients P_i and P_v needed by Star-CCM+ can be obtained through the definition of field functions on the form

$$\begin{aligned} P_i &= \mu C_i \\ P_v &= \frac{1}{2} \rho C_v \end{aligned} \quad (2.65)$$

Also, this way a temperature dependence of the porous resistance can be included via the dynamic viscosity, μ and density, ρ .

2.6.2 Single stream heat exchanger model

The single stream heat exchanger model uses only one of the actual fluid streams in a heat exchanger and assumes the other stream have a uniform temperature, T_{ref} , specified by the user. The model also requires a heat exchanger entalphy source, Q_{total} , and a minimum temperature difference, ΔT_{min} , to be specified to decide the total amount of heat transferred in the heat exchanger. Star-CCM+ calculates the local heat transfer of each cell in the heat exchanger, Q_c , from the relation

$$Q_c = Q_{total} \frac{V_c v_c (T_{ref} - T_c)}{\sum V_c v_c (T_{ref} - T_c)} \quad (2.66)$$

where V_c is the local cell volume and v_c is the local cell velocity for the modeled stream. If the uniform temperature is erroneously defined, Star-CCM+ shifts it to obtain the minimum temperature difference.

2.6.3 Dual stream heat exchanger model

In dual stream, Star-CCM+ uses both the streams to mimic the heat transfer in the heat exchanger. It does this by calculating a local energy source for each cell in the heat exchanger region and applying this as an energy sink term and source term to the hot and cold stream energy equations respectively. Star-CCM+ calculates the local energy source for each cell from the equation

$$src_i = \frac{ual_i (T_{hi} - T_{ci}) V_i}{\frac{1}{NC} \sum V_i} \quad (2.67)$$

where i denotes local cell number, ual_i is the local heat transfer coefficient, T_{hi} and T_{ci} is the hot and cold stream cell temperatures respectively, V_i is the cell volume and NC is the total number of cells in the heat exchanger.

Star-CCM+ gives several possibilities for defining the local heat transfer coefficients. Most of these options require tabulated data of velocities, mass flow rates, local heat transfer or overall heat transfer in different combinations. The *UAL Polynomial* gives the possibility to calculatate local heat transfer coefficient from the cold stream velocity alone. This is done through an equation

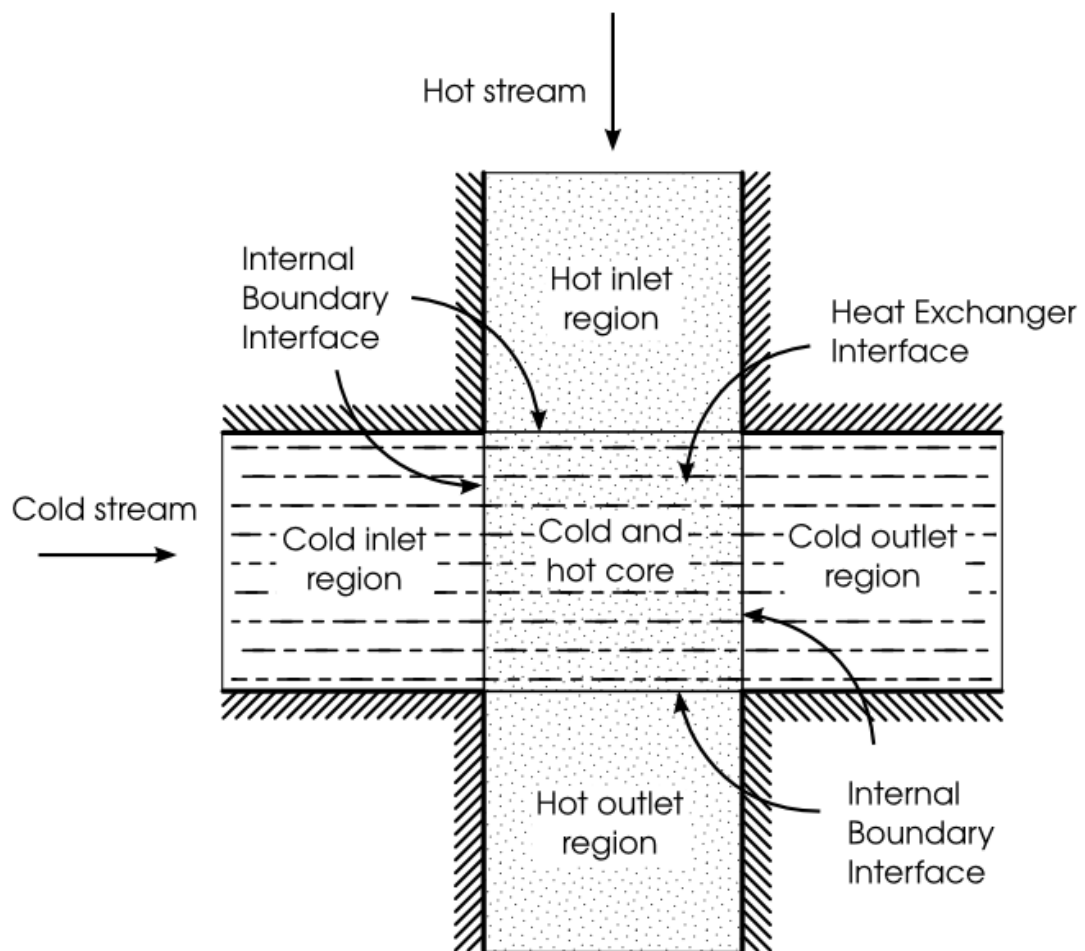


Figure 2.5: Heat exchanger topology required by Star-CCM+ for dual stream modeling.

$$UAL = \alpha + \beta v^a + \gamma v^b \quad (2.68)$$

where v is the local cold stream velocity and the number of terms as well as all the coefficients (here α , β and γ) and exponents (here a and b) can be specified.

Star-CCM+ also leaves an option to use basic dual stream heat exchanger. If chosen, Star-CCM+ solves a simplified energy equation with only the convection term for the heat exchanger domain.

2.6.3.1 Heat exchanger topology

Star-CCM+ need a specific topology setup to use the dual stream heat exchanger model. A sketch of this topology is shown in Figure 2.5. Both the hot and the cold stream need to have regions upstream and downstream of the core with an internal interface into the core region. Both of the streams also need a core region each. These core regions will be interfaced together with a heat exchanger interface (2.4.2.2). This provides the actual heat transfer capability of the model.

2.7 Modeling radiation

Star-CCM+ gives the possibility to solve the radiation transfer equation as surface-to-surface radiation, without taking the intersecting medium into account, or with participating media radiation. In addition, either grey thermal radiation or multi-band thermal radiation must be used to treat the radiative properties uniformly for the full thermal spectrum or individually for defined subspectra respectively (wavelength dependent) [4].

For the calculations, Star-CCM+ divide all surfaces into patches with the size ranging from an entire boundary down to a single element face. From the center of each patch a specified number of rays are dispatched in different directions and view factors for all the rays are calculated. For fixed properties and a fixed geometry, the view factors only have to be calculated once. Then radiation fluxes are calculated for all the patches from radiation equilibrium over all the faces in the enclosure with the use of the view factors and intensities given by the radiation transfer equation.

3

Method

This chapter describe the final chosen method of setting up and running the simulations. All the setbacks and sidetracks will not be highlighted here, but some of them are of interest and will be discussed in the next chapter.

3.1 Model preparation

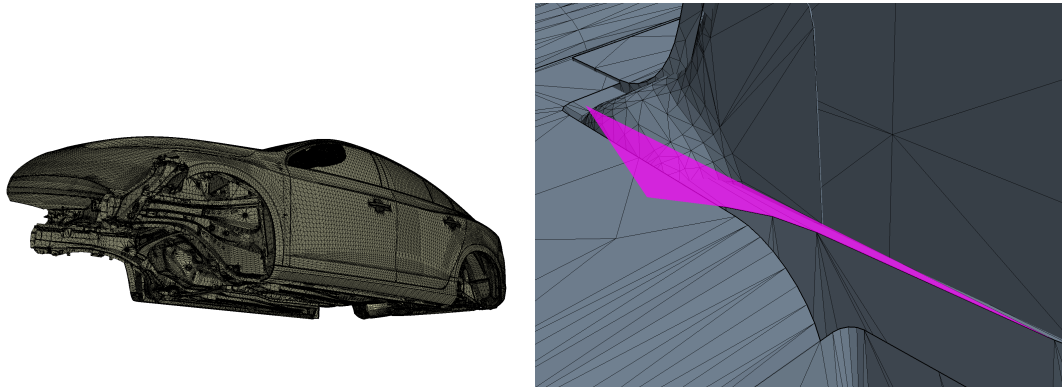
The computer model used in the simulations consists of an entire Volvo S60 in a wind tunnel, including a resolved engine bay with all its components. Due to this complex geometry, it was considered too time consuming to clean the entire geometry from errors (2.4.2). Instead, surface wrapping (2.4.2.1) were used to prepare the major part of the geometry.

Since the actual car is already on the market and not still in development, all the original CAD models, with smooth curved surfaces, could not be retrieved from the employer. Instead, part of the model was already meshed with a surface wrap tool in ANSA at delivery, with more angular surfaces as a result. The parts not already meshed were ready to be surface meshed in ANSA. To get a consistent model and an efficient way to transfer the model into Star-CCM+ with all the surface names maintained, the remainder of the model was surface meshed in ANSA too and the entire model exported as a Nastran-file and imported into Star-CCM+.

However, even though the model was prepared and able to be surface meshed in ANSA, it did not meet the requirements to be volume meshed in Star-CCM+ (2.4.2). Therefore, the model needed to be surface wrapped and remeshed within Star-CCM+ as well. Even though all the parts of the car were included in the surface wrap, some parts of the model were of special interest. So as a first step, these parts were lifted aside from the original model, to be treated separately. These steps are all described in the following sections.

3.1.1 Sealing the inside of the car

There were no apparent reasons to resolve the inside of the car to achieve good correlation of temperatures in the engine bay. Figure (3.1a) show the structures delimiting the inside of the car in the model. Star-CCM+ have several automatic tools to close gaps and holes, but since they failed at a few positions in this case, the inside had to be manually sealed off, to make sure its inner volume was not included



(a) The structures delimiting the inside of the car. (b) Manually added cell faces to seal off the inside of the car.

Figure 3.1: The inside of the car had to be manually sealed off to be excluded from the simulations.

when running the surface wrapper. To find the exact positions where seals were needed, the leak detection tool (2.4.2.1) was used. The seals were then put in place by manually adding shell elements to the model in the Star-CCM+ surface repair mode (2.4.2). One of the manually added seals is shown in Figure (3.1b).

3.1.2 Surface wrap of the car and wind tunnel

The air inside the wind tunnel surrounding the car including the air inside the engine bay surrounding the engine was the main fluid domain of the calculations. To create a region for this fluid domain, one closed and manifold surface of the wind tunnel and the car, including the engine and all the components in the engine bay and under the car, had to be created. To do this, the surface wrap tool was used. The alternative – to clean the geometry from errors at CAD level – would have taken too much time and was not a viable option for this thesis. With the surface wrap, a closed and manifold surface could be obtained relatively quickly. The cost was some lost details in the geometry. Overall, the surface wrapper uses the same algorithm as the regular meshing tool in Star-CCM+ so no major degradation of the surface should occur that would not occur anyway in the meshing stage, given that similar settings were used for the surface wrapper and the surface remesher. The difference is that the surface wrapper comes with the ability to seal small holes and gaps and that it merges surfaces from different parts together.

A balance had to be made to get a detailed enough mesh but with a number of cells low enough to be able to run calculations in a reasonable time span. Since the focus of the thesis was the the flow and temperatures in the engine bay, naturally the highest resolution was used there, with focus on the backside of the engine where the highest temperatures were expected. At the outside of the front of the car as well as under the car mid resolution was used. At the top and back of the car a lower resolutoin was used. The cell size at the wind tunnel walls were set several magnitudes larger. The parameters used are given in Table 3.1. The meshing is further described in Section 2.4.3.

Table 3.1: Target and minimum surface sizes used in the surface wrap and mesh.

Area	Target Surface Size [mm]	Minimum Surface Size [mm]
Solid parts	2	1
Turbo system	2	1
Backside of engine	2	1
Engine bay	4	2
Front of car	4	2
Under the car	8	4
Top and back of car	16	8
Wind tunnel	1000	500



(a) Cooling Fan inside the fan shroud. (b) MRF zone added around the Cooling Fan.

Figure 3.2: The MRF zone created around the fan with a small gap to the fan itself and the adjacent fan shroud.

3.1.3 Cooling fan

Moving reference frame (MRF) modeling (2.5) were used to mimic the rotation of the cooling fan. A closed volume (MRF zone) were created around the cooling fan to be simulated as a separate region. The fanflaps were subtracted (2.4.2.3) from the MRF zone to be included as solid walls. Small gaps were kept between the MRF zone and both the fan shroud and the fan itself so the MRF zone outer surfaces only had direct contact with air. Due to this, all interfaces between the MRF zone and the adjacent fluid were modeled as internal interfaces (2.4.2.2), allowing air to flow across them. To create these interfaces, while keeping the MRF zone intact, the MRF zone was included in the surface wrap of the car but as a preserved part (2.4.2.1). Finally, the MRF zone was imprinted onto the surface wrapped car to ensure conformal interfaces when performing the surface mesh.

To define the rotation of the MRF zone, a local coordinate system were created with one axis aligned with the center of rotation of the fan. A reference frame rotating around this axis could then be created and assigned to the MRF zone, with a rotational speed specified to 3072 rpm (2.5).

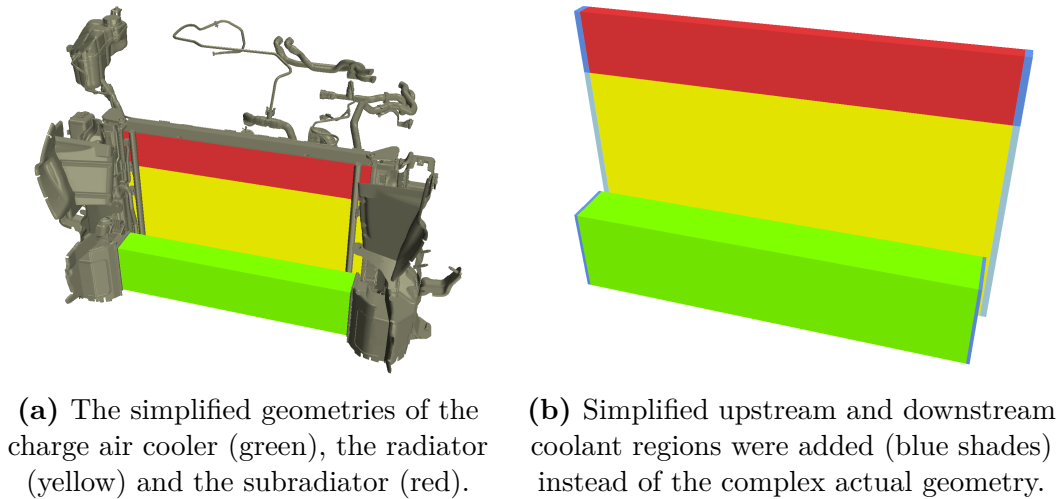


Figure 3.3: The charge air cooler, radiator and subradiator were modeled as dual stream heat exchangers and the condenser (not visible in the figures) as Single Stream.

3.1.4 Heat exchangers

The charge air cooler, radiator and subradiator where all modeled as dual stream heat exchangers (2.6.3). Simplified geometries for the heat exchanger cores were prepared in the originally recieved model (Figure 3.3a). These were kept, but one core had to be split into radiator and subradiator. After the split, the radiator and subradiator were imprinted (2.4.2.3) onto each other to diminish any gap and create a baffle interface to keep the regions separate.

The actual geometry for the upstream and downstream coolant flow was included in the original model. These geometries were included in the surface wrap of the car, but was considered too time consuming to clean from errors to be used for the dual stream coolant flow. Instead, thin extentions where added at both sides of each of the heat exchanger cores to create the upstream and downstream regions needed for the coolant flow (Figure 3.3b). This was done to achieve the heat exchanger topology required for dual stream modeling (2.6.3).

All the heat exchangers cores were included in the surface wrap of the car to allocate their volumes in the main fluid domain, but they were meshed seperately to create their internal volumes. Two identical cores are needed in the dual stream heat exchanger model, as further described in Section 2.6. Only one core per heat exchanger, together with all the upstream and downstream regions, were included when meshing the heat exchangers. The cores were duplicated after meshing to provide two identical cores for each heat exchanger, one for the coolant flow and one for the air flow. All the core, upstream and downstream regions were then connected according to the topology described in Section 2.6. At the top and bottom of the cores, baffle interfaces were used to the delimit the cores from the adjacent fluid with no heat transfer occuring.

Beside dual stream, the heat exchanger air cores were modeled as porous regions (2.6) to capture the pressure loss through the heat exchangers. Porous inertial

and viscous coefficients were provided for each of the heat exchangers as C_i and C_v according to Equation 2.63. To use these in Star-CCM+, field functions were created according to Equation 2.65.

The simulations were run with constant density, which imply a constant dynamic viscosity (dynamic viscosity = density * kinematic viscosity). However, the dynamic viscosity could be expected to vary enough to have an impact on the porous resistances of the heat exchangers. To include this variation without having to run the entire simulation with varying density (which demands more computational time) the dynamic viscosity was calculated using Sutherland's law

$$\mu = \mu_{ref} \left(\frac{T}{T_{ref}} \right)^{3/2} + \frac{T_{ref} + S}{T + S} \quad (3.1)$$

which gives the dynamic viscosity from the temperature, T , the Sutherland temperature, S , and a reference dynamic viscosity, μ_{ref} , taken at a reference temperature, T_{ref} . The coefficient values for air are given in Table 3.2.

Table 3.2: Coefficient values for Sutherland's law for air.

μ_{ref} [Pa s]	T_{ref} [K]	S [K]
1.71610^{-5}	273.15	111.0

For the coolant flows, only the mass flow and temperature were of interest, so the coolant flows were modeled as a regular flow with no porous effects.

No elaborate data was provided of the running conditions for the condenser apart from its porous resistance and an estimation of a total effect of 5 kW. Therefore the condenser was modeled as a single stream heat exchanger with the heat exchanger enthalpy source specified to 5 kW at a uniform coolant temperature of 350 K.

3.1.5 Components for temperature comparison

Several components were appointed by Volvo as suitable for comparing temperatures between the calculations and tests in order to be able to verify the accuracy of the simulations. These are shown in Figure 3.4 and a list of the components are given in Table 3.3 along with the material data used. These components were still included in the surface wrap of the car, but also lifted aside and prepared to be volume meshed separately and included as solid parts in the simulations. These parts were cleaned with the aid of either ANSA or Star-CCM+ to meet the requirements for volume meshing in Star-CCM+. Two of them - the cam belt cover and a part of the cabin heater hose - were considered too complicated to prepare manually and were therefore surface wrapped individually. In these cases, not the original, but the wrapped surfaces, were included in the surface wrap of the car. When surface wrapping the car, the option to create weak in-place contacts with input parts were selected. The resulting contacts ensured that interfaces were created between the fluid volume and the solid parts.

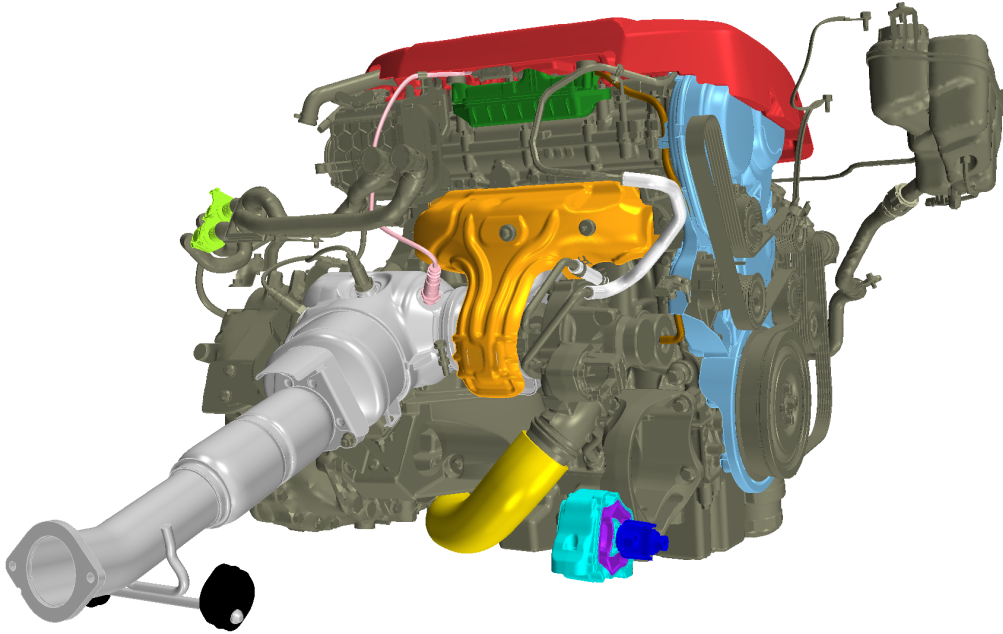


Figure 3.4: The components selected for temperature comparison. Manifold Heat Shield (orange), Cabin Heater Hose (light green), Engine Cover (red), Cam Belt Cover (light blue), Vacuum Hose (brown), Vacuum tank (dark green), Lambdasond (pink), Turbo Cooling Hoses (white), Charge Air Hose (yellow), Exhaust Hangers (black), MUPP Rubber (purple), MUPP Bracket (blue), MUPP Shell (cyan), Exhaust system (grey).

Table 3.3: Components for temperature comparison along with the material data used.

Component	Material	Thermal cond.	Emissivity
Manifold Heat Shield	Aluminum	201.07	0.22
Manifold Heat Shield Insul.	Elotherm	0.07	0.22
Cabin Heater Hose	Polyethylene	0.40	0.92
Engine Cover	Polyethylene	0.09	0.91
Cam Belt Cover	Polyethylene	0.40	0.92
Vacuum hose	Rubber	0.23	0.92
Vacuum tank	Polyethylene	0.30	0.92
Lambdasond Cable	Rubber	0.16	0.92
Lambdasond Bushing	Steel	52.02	0.60
Lambdasond Sond	Stainless Steel	18.69	0.60
Turbo Cooling Hoses	Steel	52.02	0.50
Charge Air Hose	Polyethylene	0.40	0.92
Exhaust Hangers	Rubber	0.16	0.92
MUPP Rubber (TK252)	Rubber	0.16	0.92
MUPP Bracket (TK257)	Steel	52.02	0.91
MUPP Shell (TK253, 254)	Aluminum	201.07	0.50

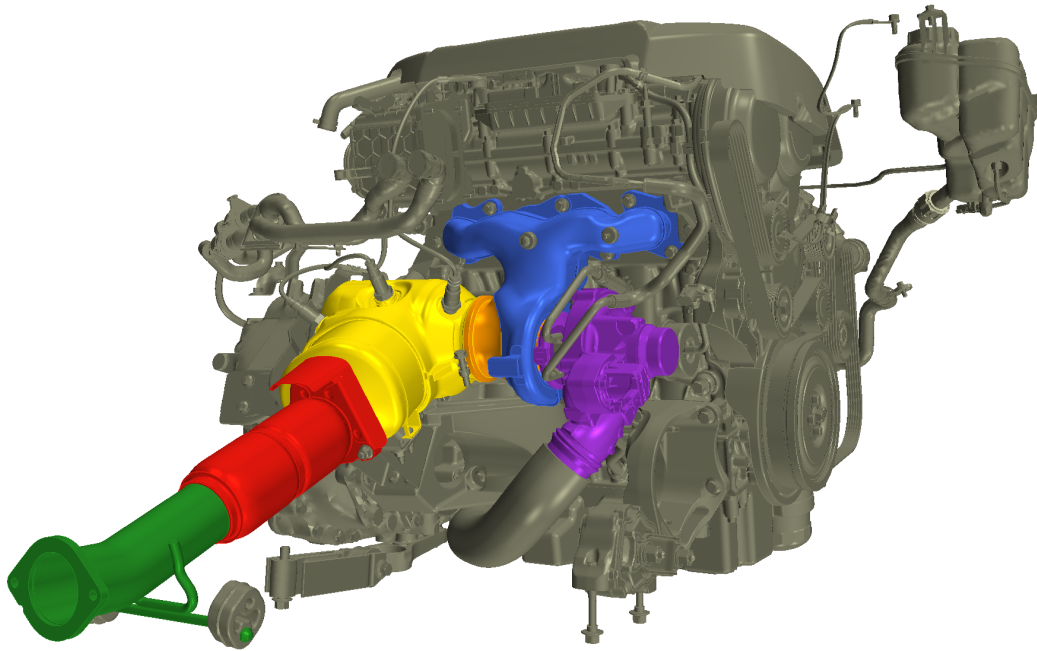


Figure 3.5: The solid parts surrounding the exhaust gases.

The manifold hHeat shield required some extra attention. The shield is composed of two thin aluminum sheets with an insulating material in between. When produced, these three sheets are pressed together with possible thin air pockets and varying thicknesses as a result. In the CAD file this component was represented by a surface with no thickness. This was inflated and divided into the three layers present in the actual component. The two aluminum sheets were made with 0.4 mm of thickness and the insulating material in the middle with 0.5 mm of thickness.

3.1.6 Internal exhaust flow

To capture the heat distribution in the engine bay properly, the hottest area, namely the internal gas flow, was simulated from the inlet of the exhaust manifold (blue in Figure 3.5), through the turbocharger (purple), the exit flange (orange), the catalytic converter (yellow), flexpipe (red) and exhaust pipe (green). The solid parts delimiting the exhaust flow were included in the simulations as solids. To set this up, the solids were cleaned and the internal exhaust volume created in ANSA. The solids were then meshed separately in Star-CCM+, but also included in the Surface Wrap of the car to allocate their space in the main fluid volume and create interfaces with the same. The right part of the turbocharger does not hold exhaust gases but charge air, so neither its internal volume or the solids were included in the simulation with volume meshes. Only the turbine wheel and turbine wheel housing located inside the bottom of the Manifold were included.

Parts	Region	Mesh
Wind Tunnel	Fluid Volume	Automated Mesh
Car		
Fan MRF Zone		
Solid components	Solids	Solid mesh
Cam Belt Cover	Solids.Cam Belt Cover	
Powertrain mounts	Powertrain mounts (8 regions)	
Exhaust system	Manifold-turbo-exhaust	
Heat Exchangers (HXC's)	HXC Cores (4 region)	HXC
HXC's Up-/Downstream	HXC Up/Down (3 regions)	

Table 3.4: The division of parts into regions and their used mesh processes. The Automated Mesh was performed as parts-based mesh operation, while the Solid and HXC meshes were performed with a region-based mesh continua.

3.1.7 Meshing

The computational domain could be divided into a number of categories, namely the main fluid domain, the heat exchangers, the solids of the exhaust system, the exhaust gases of the exhaust system and the solid components included for temperature comparison with the tests. These were treated differently in the meshing procedure and meshed with separate operations/mesh continua. The division of parts into regions and their meshing procedure are shown in Table 3.4.

Table 3.5: Parameter values used for the main fluid automated meshing

Parameter	Value
Base Size	32.0 mm
CAD Projection	Disabled
Target Surface Size	100.0%
Minimum Surface Size	50.0%
Surface Curvature	36.0 Pts/circle
Surface proximity	2.0 mm, 2.0 points in gap
Surface growth rate	1.3
Auto-Repair Minimum Proximity	0.01
Number of Prism Layers	3
Prism Layer Stretching	1.5
Prism Layer Total Thickness	33.0% = 10.56 mm
Mesh Density	Density 1.0, Growth Factor 1.0

From the advantages described in Section 2.4.3 a polyhedral volume mesh was chosen to be used for a majority of the calculation domain. The main fluid domain was meshed with a regular polyhedral mesher. Prism layers were also used to try to capture the boundary layer effects. To obtain conformal interfaces between the fan MRF zone and the main fluid domain, these were meshed with the same mesh operation.

Since the the flow direction can be well predicted for the major part of the inter-

Table 3.6: Parameter values used for the solids automated meshing

Parameter	Value
Base Size	2.0 mm
Auto-Repair Minimum Proximity	0.05
Auto-Repair Minimum Quality	0.01
CAD Projection	Enabled
Surface Curvature	36.0 Pts/circle
Surface growth rate	1.3
Surface proximity	1.0 mm, 2.0 points in gap
Target Surface Size	100.0%
Minimum Surface Size	50.0%
Thin Mesher Layers	2

nal exhaust gas flow, this region were meshed with hexahedral cells aligned in the expected flow direction. Prism layers were used here too to capture the boundary layer.

The solids of both the turbo system and the components for temperature comparison were meshed with the so called *thin mesher*, but still with the use of polyhedral elements. The Thin Mesher can be used in combination of any other element type, but it locates thin structures from a defined thickness parameter and adds extra elements. The result looks similar to a prism layer mesh, but with even distribution instead of growing cell heights.

Table 3.7: Parameter values used for the heat exchangers automated meshing

Parameter	Value
Base Size	4.0 mm
Auto-Repair Minimum Proximity	0.05
Auto-Repair Minimum Quality	0.01
CAD Projection	Enabled
Maximum Cell Size	150%
Mesh Alignment Location	[0.0, 0.0, 0.0] m
Surface Curvature	36.0 Pts/circle
Surface growth rate	1.3
Surface proximity	0.0 mm, 2.0 points in gap
Target Surface Size	100.0%
Minimum Surface Size	50.0%
Template Growth Rate	Fast
Boundary Growth Rate	None

Since the flow in the heat exchangers is highly restricted in direction, a hexahedral mesh aligned with the flow was used here as well. This prohibited the creation of conformal interfaces (2.4.2.2) to the main fluid domain, but since only weak in-place contacts were created via the use of the surface wrapper, conformal interfaces was not guaranteed anyway.

Table 3.8: Parameter values used for the internal exhaust gas automated meshing. Numbers for the area surrounding the turbine wheel are given in brackets.

Parameter	Value
Base Size	2 mm (0.5 mm)
CAD Projection	Enabled
Maximum Cell Size	2 mm (0.5 mm)%
Number of Prism Layers	3 (1)
Prism Layer Stretching	1.3 (1.5)
Prism Layer Thickness	2 mm (1.25 mm)
Surface Curvature	36.0 Pts/circle
Surface growth rate	1.3
Surface proximity	0.0 mm, 2.0 points in gap
Target Surface Size	2 mm (100%)
Minimum Surface Size	1.8 mm (100%)
Template Growth Rate	Medium
Boundary Growth Rate	None

The mesh generation is automatic in Star-CCM+ but there are several parameters to be specified to control the outcome of the mesh generation. The majority of the parameters are used to directly control the outcome of the surface mesh generation and only indirectly the volume mesh since it is created to match the surface mesh. As previously stated, similar parameters were used for both the surface wrap and the surface mesh, to avoid unnecessary degradation of the surface. The target and minimum surface sizes for all but the internal exhaust gases are given in Table 3.1. These were applied using so called surface controls, which gives the possibility to assign values to specified boundaries in a region (while the parameters in general apply to an entire region). The additional parameters used in the meshing process are given in Table 3.5, 3.6, 3.7 and 3.8 for the different meshes. The base size, target surface size and minimum surface size from Table 3.5 were not really in use, since all surfaces were targeted with surface controls. For the solids and the heat exchangers, per-region meshing was used. This means every region is meshed separately with no conformal interfaces in between.

All in all this meshing procedure rendered a mesh of 56.5 million cells (excluding the internal exhaust gases) and 2.7 million cells for the internal exhaust gases.

It is common that a number of invalid cells occur when meshing complex volumes in Star-CCM+, so also in this case. Simulations can not be run with these cells included. As a remedy, these cells were lifted aside with the remove invalid cells command. This command can remove cells according to several different criteria, for example cell quality and volume change. In this case, only cells with zero or negative volume were removed. Symmetry planes are added to the faces neighbouring the removed cells.

Table 3.9: Models and physics included at different stages of the simulation process.

Heat exch.	Fan	Solids	Exhaust	Turb.	Energy	Radiation
Absent	Stationary	Surface	No	$k - \omega$	No	No
Porous	MRF	Surface	No	$k - \omega$	No	No
Single str.	MRF	Surface	No	$k - \omega$	Yes	No
Dual str.	MRF	Surface	No	$k - \omega$	Yes	No
Dual str.	MRF	Solid	Yes	$k - \omega$	Yes	Yes

3.2 Simulation setup

Due to the complex geometry and physics of the task, the simulation complexity was gradually intensified to finally reach the level of the main simulation. This means the chronological order presented in the report with first meshing and then simulating was actually a back and forth work until the final complexity of the entire simulation was reached. The first simplified simulations are here called the *early simulations*. When all the geometry and physics had been added and stability in the calculations confirmed, focus was turned to adjusting different parameters of the simulation to improve the results. This stage is refer to as the *main simulation*.

3.2.1 Early simulations

Instability was a foreseen possible issue within the calculations due to the complex geometry and complexity of the physics (two fluid domains, solids, heat exchangers, heat transfer including radiation etcetera). To try to isolate stability issues at an early stage, the calculations were made as simple as possible to begin with, and complexity added in stages. At first, the plain surface wrapped geometry were used with the heat exchangers absent, the cooling fan stationary, the standard settings of steady state $k - \omega$ solver used with no energy or radiation equations solved. When this calculation were confirmed stable to run, the cooling fan were added as an MRF zone and the heat exchangers as porous regions and the calculations were continued. The calculations were then advanced according to the setups given in Table 3.9.

The last row of Table 3.9 can be considered to be the first main simulation. Only at this stage at first were the solids and exhaust system included with volume mesh as well as the internal exhaust gas flow calculations included as convective boundary conditions at the inner surface of the exhaust system.

3.2.2 Main simulation

The models and physics used for the main simulation is given in the last row of Table 3.9. The solvers used for the different regions are listed in Tables 3.10 and 3.11. At the time of simulation setup, it appeared the k-omega turbulence model could not be chosen for the RAD/SUB and therefore realizable k-epsilon was used in this case.

Table 3.10: Solvers used in the main simulation for the main fluid region and solid regions.

Air (main fluid)	Solids
All y+ Wall Treatment	Cell Quality Remediation
Cell Quality Remediation	Co-Simulation
Constant Density	Constant Density
Gas	Gradients
Gradients	Multi-Part Solid
Gray Thermal Radiation	Segregated Solid Energy
K-Omega Turbulence	STAR-CCM+ Steady Co-Simulation
Radiation	Steady
Reynolds-Averaged Navier-Stokes	Three Dimensional
Segregated Flow	
Segregated Fluid Temperature	
SST (Menter) K-Omega	
Steady	
Surface-to-Surface Radiation	
Three Dimensional	
Turbulent	
ViewFactors Calculator	

Table 3.11: Solvers used in the main simulation for the Radiator, Subradiator and Charge Air Cooler regions.

RAD/SUB	CAC
Cell Quality Remediation	All y+ Wall Treatment
Constant Density	Cell Quality Remediation
Gradients	Constant Density
K-Epsilon Turbulence	Gas
Liquid	Gradients
Realizable K-Epsilong Two-Layer	K-Omega Turbulence
Reynolds-Averaged Navier-Stokes	Reynolds-Averaged Navier-Stokes
Segregated Flow	Segregated Flow
Segregated Fluid Temperature	Segregated Fluid Temperature
Steady	SST (Menter) K-Omega
Three Dimensional	Steady
Turbulent	Three Dimensional
Two-Layer All y+ Wall Treatment	Turbulent

Table 3.12: Boundary conditions used. To protect sensitive data temperatures are normed with the same constant temperature as in the contour plots in Chapter 4.

Boundary	Boundary Condition
Wind Tunnel Inlet	Velocity inlet, 70 km/h (ramped)
Wind Tunnel Outlet	Flowsplit outlet
Wind Tunnel Floor	Translational motion, 70 km/h
Wind Tunnel Roof & Walls	Slip
Higher Cylinder Head, rear side	Static temperature, 0.807
Lower Cylinder Head, rear side	Static temperature, 0.875
Cylinder Block, rear side	Static temperature, 0.825
Oil Sump, rear side	Static temperature, 0.825
Super Charger	Static temperature, 0.744
Gearbox, rear side	Static temperature, 0.799
Front of engine and gearbox	Static temperature, 0.766
CAC Coolant Upstream Inlet	Massflow inlet, Temperature, 0.780
CAC Coolant Downstream Outlet	Flowsplit outlet
Radiator Coolant Upstream Inlet	Massflow inlet, Temperature, 0.774
Radiator Coolant Downstream Outlet	Flowsplit outlet
Subradiator Coolant Upstream Inlet	Massflow inlet, Temperature, 0.774
Subradiator Coolant Downstream Outlet	Flowsplit outlet
Cabin Heater Hose Interior	Convection, Temperature, 0.773 Heat Transfer Coeff, $146W/m^2K$
Turbo Cooling Inlet Interior	Convection, Temperature, 0.764 Heat Transfer Coeff, $231W/m^2K$
Turbo Cooling Outlet Interior	Convection, Temperature, 0.773 Heat Transfer Coeff, $244W/m^2K$
Charge Air Hose Interior	Static Temperature, 0.780

The initial conditions were left as standard values except for the velocity of the main fluid domain which was set to 0.1 m/s in the streamwise directions. This to avoid large volumes with zero velocity, which is prone to cause trouble. To avoid instability problems when starting the calculations the inlet velocity was ramped up from 0 to 70 km/h with a field function on the form

$$\begin{aligned} \frac{70}{3.6} \frac{i^{1/3}}{50^{1/3}}, i \leq 50 \\ \frac{70}{3.6}, i > 50 \end{aligned} \quad (3.2)$$

where i denotes the number of iterations performed. This gives a large increase of the inlet velocity in the beginning which then levels out towards 70 km/h.

The boundary conditions used are specified in Table 3.12. For the boundary conditions not specified in the table, standard setting boundary conditions were used, which mean adiabatic, no-slip, stationary and emissivity 0.8.

To mimic the heat transfer in the dual stream heat exchangers (radiator, subradiator and charge air cooler), the UAL Polynomial approach was chosen for calculating the local heat transfer coefficient. It was chosen for its easy implementation but also for the minimal need of input data. With the inlet massflow and temperature of the coolant flows given as stated in Table 3.12, the polynom was adjusted for the heat exchangers to achieve an outlet coolant temperature matching the temperatures from the tests. The final polynoms used was

$$UAL = C + Cv + Cv^2 \quad (3.3)$$

where UAL is the local heat transfer coefficient, v is the cold stream velocity and the coefficient, C , where set to $C = 0.02$ for the Charge Air Cooler and $C = 0.11$ for the Radiator and Subradiator.

Following an advice from CD-Adapco (manufacturer of Star-CCM+), a couple of parameters of the SST $k-\omega$ solver were adjusted. The A1 coefficient was raised to 1 (from 0.31), the realizability coefficient was raised to 1.2 (from 0.6) and the compressibility correction was deactivated. Adjusting the A1 coefficient should counteract a problem of erroneous early separations of the flow. All in all these adjustments are suggested to lead to better stability.

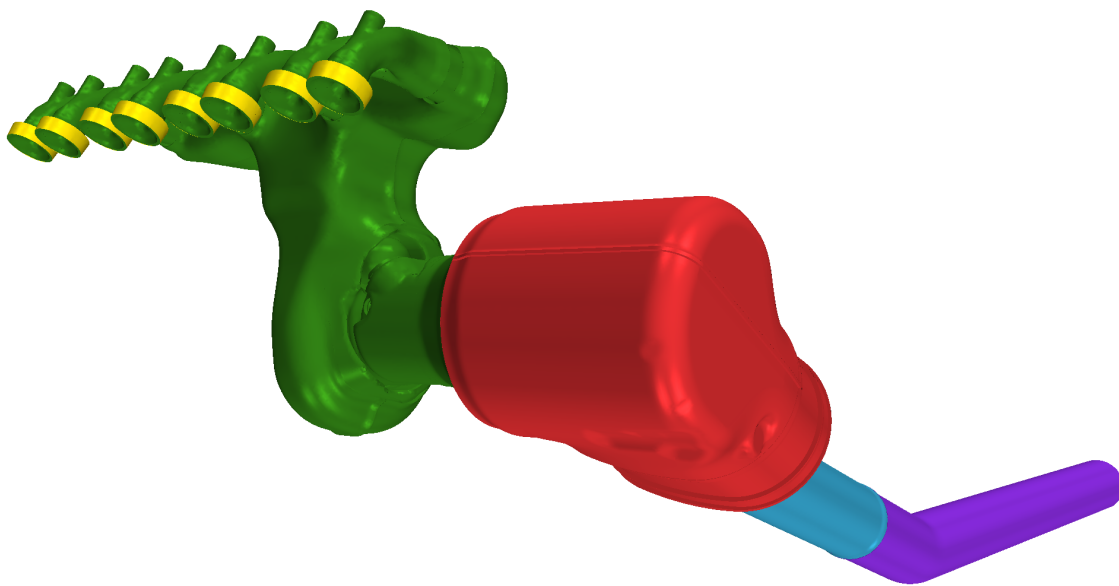
The parameters used for the view factor calculations and surface to surface radiation are given in Table 3.13. A patch/face proportion value of 50% was also tested for the surfaces of the solid components (including the exhaust system) to rule out this parameter out as a possible error source.

3.2.3 Internal exhaust gas simulation

To not complicate the simulation setup, calculations of the internal exhaust flow was ran as a separate transient simulation to begin with. The internal exhaust gas

Table 3.13: Parameter values for the view factor calculation and surface to surface radiation

Parameter	Value
Number of Beams	1024
Maximum Reciprocity Iterations	100
Reciprocity Tolerance	0.001
Maximum Polygons per Voxel	50
Radiation Temperature	300 K
Patch/Face Proportion (in engine bay)	5%
Patch/Face Proportion (away from engine bay)	1%

**Figure 3.6:** The internal exhaust gas flow. The four pairs of inlets are coloured yellow, the manifold green, catalytic converter red, the flexpipe blue and the exhaust pipe purple.

simulation and the main simulation were alternately ran three times and results exported as tables with spatial coordinates and included as boundary conditions in the other calculation. However, the results varied substantially between the second and third run, so after this the internal exhaust simulation was adjusted to steady state and included in the main simulation via co-simulation. A view of the internal exhaust gas flow domain is given in Figure 3.6. The four pairs of inlets are coloured yellow. The exhaust pipe was extended to avoid influence on the results from the pressure outlet.

3.2.3.1 Separate transient simulation

The internal exhaust gas simulation were ran as a transient simulation for about fifteen complete 360 degree revolutions of the crankshaft. Mean values of the variables were calculated during this calculation and exported to the main simulation. For

Table 3.14: Boundary conditions used for the steady state internal exhaust gas flow co-simulation. The temperature is normed with the same constant temperature as in the contour plots in Chapter 4.

Boundary	Boundary Condition
Turbine Wheel	Adiabatic
All other walls	Temperature from Co-Simulation
Inlets (4 pairs)	Massflow inlet, Temperature 1.887
Outlet	Pressure outlet

the first calculations of the internal exhaust gases, adiabatic boundary conditions were used at the outer walls. During the second and third run, surface temperatures were imported from the main simulation.

From the internal exhaust gas calculations the outer wall ambient temperature and heat transfer coefficients were exported and included in the main calculation as convective boundary conditions on the inner wall of the exhaust system. From the main calculation the temperature at the inner exhaust system walls were exported and included in the internal exhaust gas calculation as temperature boundary condition on the outer walls.

In the transient exhaust gas calculations the turbine wheel, turbine housing and catalytic substrate walls were kept as adiabatic. For the rest of the walls, adiabatic boundary condition was used for the first run. For the second and third run the temperature was specified with the spatially tabulated data imported from the main simulation. At the four pairs of inlets, massflow boundary conditions were used with the massflow and temperatures specified with time dependent tabulated data delivered from Volvo Cars.

The models and solvers used for the transient exhaust gas simulation are the same as for the air given in Table 3.10, except instead of constant density, ideal gas was used and instead of steady, implicit unsteady was used.

3.2.3.2 Steady state co-simulation

Since the result varied substantially between the second and third transient simulation, the simulation was modified to a steady state internal exhaust gas flow and included in the main simulation as a co-simulation. This way each simulation could be run 20 iterations at a time, before passing the results to its co-simulation partner. The models and solvers used for this part of the simulation are the same as for the air given in Table 3.10, except instead of constant density, ideal gas was used. The boundary conditions used are given in Table 3.14.

4

Result and Discussion

Here the results are presented. As stated earlier the goal was to correlate the calculations with experimental data from tests. Wind tunnel tests have been performed at Volvo Car Corporation by Volvo Car Corporation and the results delivered as tabulated data. To protect sensitive data, all results here are given as normed temperatures. Two different ways of normalizing the temperatures are used. The temperatures in the contour plots (colorful figures) are normed with one and the same constant temperature. The temperatures in the charts and tables are normed with the measured temperature for the respective measure point. In the later case this means a temperature higher than unity indicate overprediction in the calculations while a temperature less than unity indicate underpredicted calculations.

4.1 Temperature comparison

The main procedure to establish how well the calculations correlate with the measured data is to compare the temperatures of the appointed solid components. An overview of the temperature distribution in the exhaust system and the selected components are shown in Figure 4.1. The results show a relatively good agreement in temperature between calculations and measurements for some of the components, while other components show significant deviations. The results for the different components will be discussed in the following sections.

4.1.1 Affecting processes

Before studying the temperature comparison of the selected components, it may be interesting to evaluate the performance of the internal exhaust gas flow modeling and the heat exchanger modeling.

4.1.1.1 Internal exhaust gas flow

In Table 4.1 three temperatures of the internal exhaust gas flow are compared. The results show an underprediction of the temperature in beginning of the flow while showing overpredictions of the temperature further downstream, but overall the temperatures are close to those in the tests. However, these numbers should only be used as an indication since a discrepancy in the geometry was discovered at a late stage of the project. The catalytic converter used in the calculations is not the same

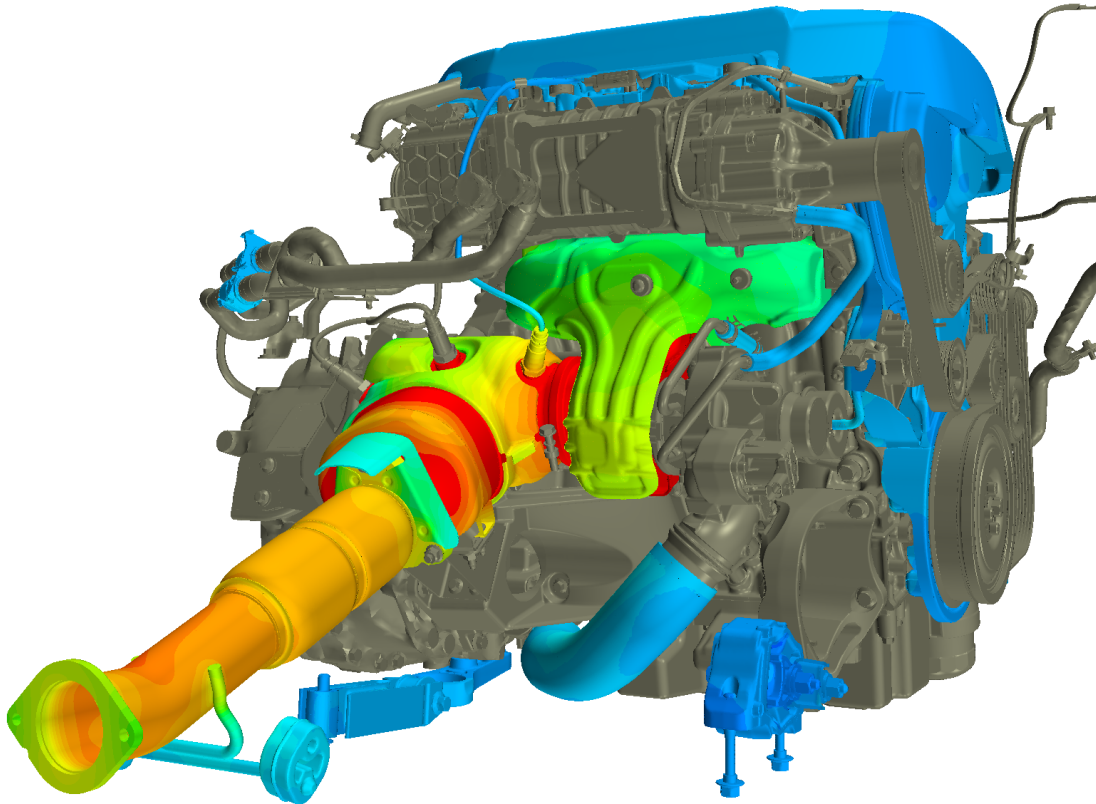


Figure 4.1: Overview of the engine. The exhaust system and components for temperature comparison are shown with temperature distribution.

Table 4.1: Temperatures for the exhaust gases normed with their respective measured result.

Position	Normed temperature
Before Turbo Compressor	0.986
Before Catalytic Converter	1.053
After Catalytic Converter	1.045

Table 4.2: Temperatures of the dual stream heat exchanger coolant outlets along heat transfer rates for the respective heat exchanger. All results are normed with respective test results.

Heat exchanger	Outlet temp	$\dot{Q}_{\text{simulation}}$ [kW]
Charge Air Cooler	0.744	1.13
Radiator	0.989	1.33
Subradiator	0.969	1.45

one used in the tests. Also, the exact location and way of measuring differ between the calculations and the tests. In the calculations, the temperature before the turbo is taken as a surface average just before the exhaust gases enter the turbine. The temperature before the catalytic converter is taken as a surface average at the inlet of the first catalytic substrate and the temperature after as a surface average at the outlet of the second substrate. The actual catalytic converter used in the test only have the first catalytic substrate.

4.1.1.2 Dual Stream heat exchangers

In Table 4.2 the normed outlet coolant temperatures of the three dual stream heat exchangers are given. As stated earlier, the inlet coolant massflow and temperature was known from tests, so the outlet coolant temperature should give a good idea of how well the dual stream models perform. The outlet temperatures of the radiator and subradiator are close to those in the test, while the outlet temperature of the charge air cooler (CAC) is significantly lower. Table 4.2 also show heat transfer rates given from the simulations and calculated from the test results with the formula $\dot{Q}_{\text{test}} = \dot{m}_{\text{in}} c_p (T_{\text{out}} - T_{\text{in}})$ where \dot{m}_{in} is the coolant inlet massflow and a specific heat capacity of $c_p = 1.009$ kJ/kg K was used for the air in the CAC and $c_p = 3.559$ kJ/kg K was used for the radiator (RAD) and subradiator (SUB) coolant, taken from tabulated data of 50% water/ethylene glycol mixture. These result show that, despite the small temperature difference, the deviation in heat transfer rate is quite extensive in both the RAD and SUB. The error is actually smaller in the CAC due to low mass flow and specific heat. To improve the accuracy of the calculations, the UAL Polynom would need to be adjusted for all three heat exchangers. As for now, they are all transferring too much heat to the air flowing into the engine bay.

4.1.2 Manifold Heat Shield

The manifold heat shield could be expected to be one of the hardest component to achieve good correlation for due to its close proximity to one of the hottest components and its complex structure and manufacturing process (3.1.5). The temperature distribution along with the placement of the measure points on the manifold heat shield are shown in Figure 4.2e and 4.2f. The normed temperatures from the measure points on the manifold heat shield are shown in Figure 4.3, divided into two graphs showing the inside of the shield (facing the manifold) and the outside of the shield (averting the manifold) respectively.

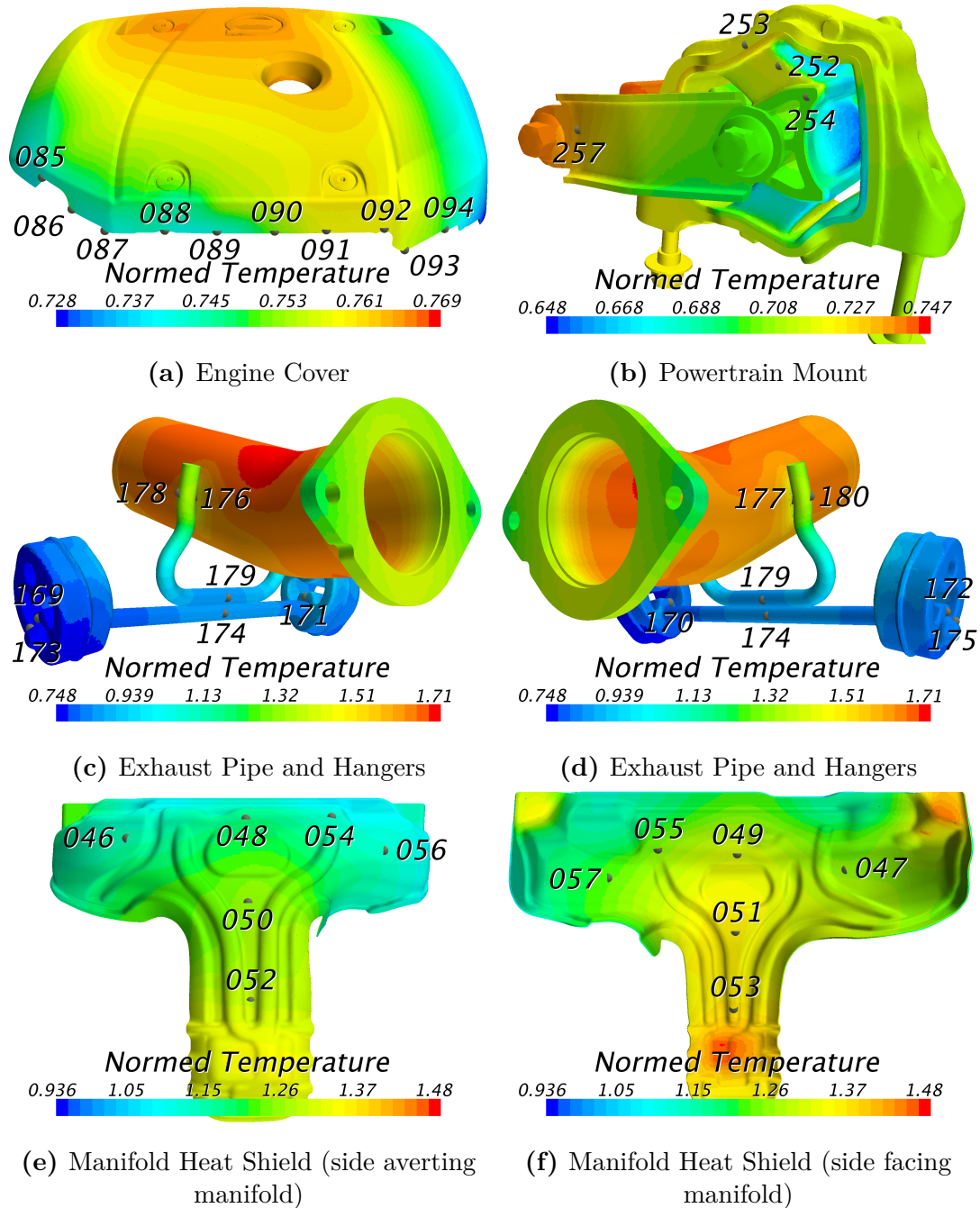


Figure 4.2: Temperature distributions for selected components in the engine bay. Measure point placements are shown in the figures with dots and numbers.

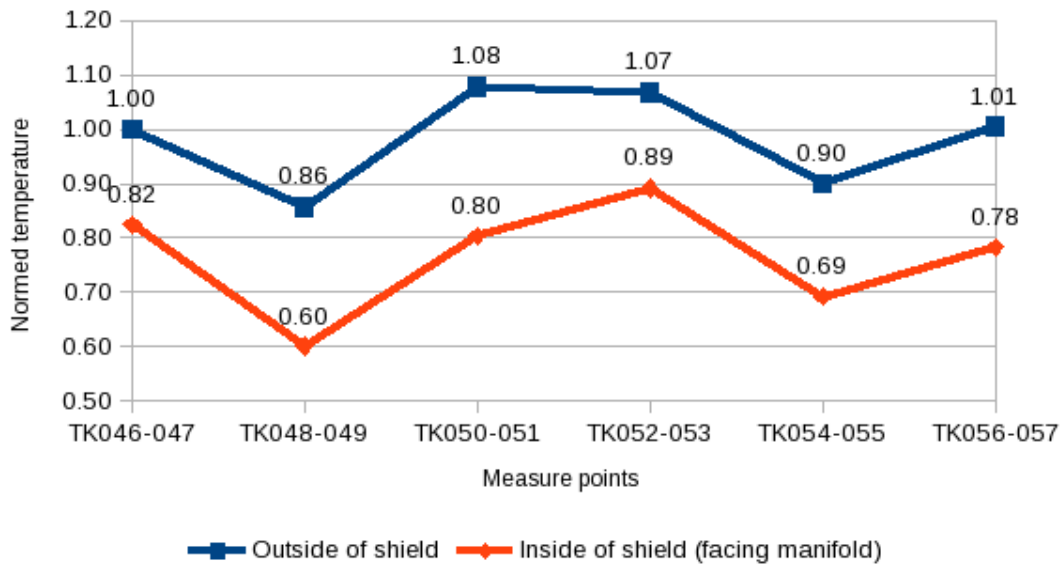


Figure 4.3: Temperatures for the measure points at the manifold heat shield, normed by their respective measured temperature.

The first impression from the results is the severe underprediction of temperatures on the inside of the shield. These are the largest deviations from the measured temperatures in the calculations. One aspect likely to have some impact on the results is the actual distance between the manifold and the manifold heat shield. A nominal distance is used in the CAD model, which is the thought distance between the two components. However, this distance is likely to be altered. The exhaust manifold is going to expand from its high working temperature (around 1000°C) moving its surface closer to the heat shield. The exact mounting of the manifold heat shield may differ from one car to the other since the shield is a thin and flexible component. In this case, extra work with and around the heat shield have been performed when placing the sensors for measuring the temperatures in the tests, possibly altering its position. Also, in the delivered CAD-model, the heat shield was represented by a surface with no thickness which had to be inflated to assume the right shape. This too altered its position relative to the manifold.

A simple simulation test was performed using Star-CCM+ with two flat plates facing each other. A static temperature similar to the manifold surface temperature was assigned to one of the plates while the resulting temperature on the second surface due to radiation was observed. The temperature varied with more than a hundred degrees celsius from 0.5 mm to 20 mm distance between the plates. The full results are shown in Figure 4.4. The distance between the Manifold and the Manifold Heat Shield is typically between 8 and 18 mm, so with these results, an altered distance may explain a part of the temperature deviations.

Another possible source of error is the surface temperature of the manifold. As shown earlier, the exhaust gas temperature was slightly underpredicted in the beginning of the exhaust gas flow, but close to the tests. Data for comparing the temperatures on

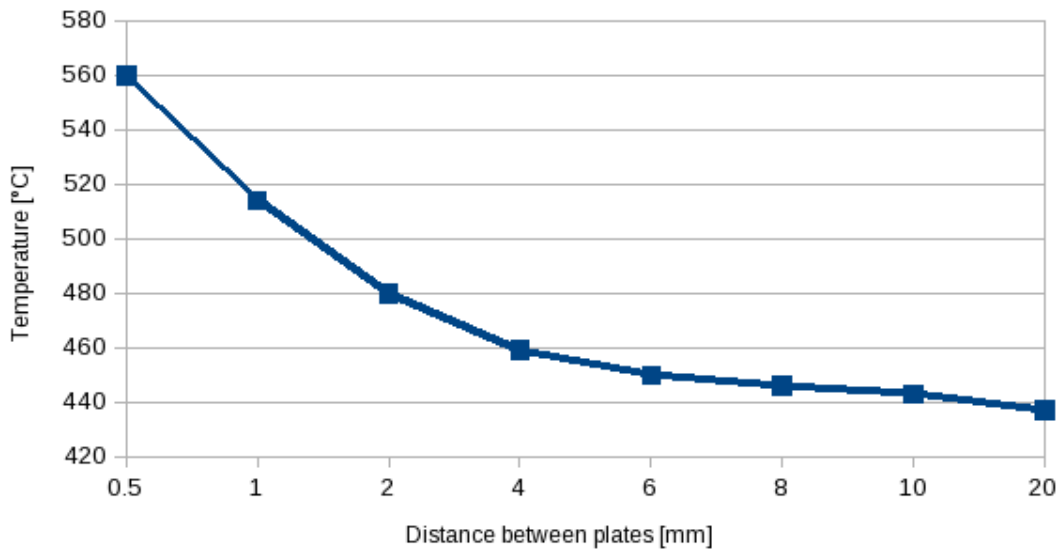


Figure 4.4: The effect of radiation was tested with a simple simulation of two flat plates facing each other.

the surface of the manifold have not been available during this project. The manifold in question is double jacketed, meaning a void exist between the inner pipes and the outer shell of the manifold where only a small fraction of the exhaust gas enter and with low velocity. This geometry is included in the simulations, but it is not properly investigated how it affects the outside manifold surface temperature. This temperature may be deviating more than the compared exhaust temperatures.

Since a quite low number was used to specify the patch/face proportion for the radiation (5%) a an extra test simulation was run where this parameter was changed to 50% for all the solid components including the entire exhaust system. This test showed no difference in results, so the low patch/face proportion can be ruled out as an error source.

The outside of the manifold heat shield (averting the manifold) show relatively good correlation with the test data even with the temperatures on the inside of the shield deviating a lot. Naturally the outside will not be as sensitive to the temperature of the manifold since the two sides of the shield are well insulated from each other (apart from at its perimiter and anchor points). Also, the outside is not facing any hot close surfaces and the heat transfer due to convection is likely higher than on the inside due to higher flow velocities. However, to fully capture the heat distribution of the manifold heat shield, the correlation of the temperatures on the inside must be improved and this will of course affect the outside as well.

With the temperatures on the inside of the shield deviating a lot, the results for the outside is not fully reliable. One conclusion to be drawn is that the outside is not at all as sensitive as the inside since the two sides are well insulated from each other, the outside is not facing any close hot surfaces and the heat transfer due to

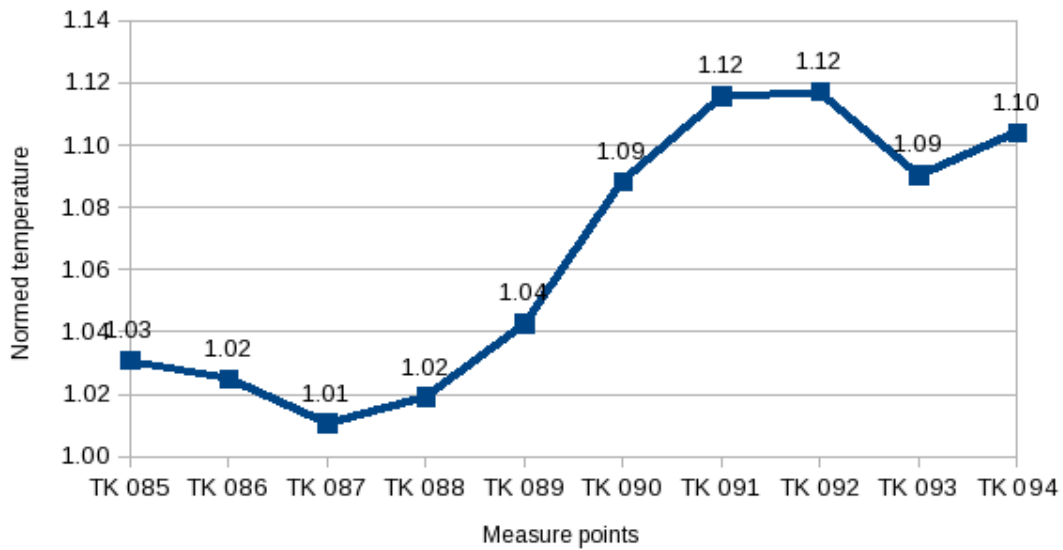


Figure 4.5: Temperatures for the measure points at the engine cover, normed by their respective measured temperature.

convection is likely higher on the outside due to higher flow velocities.

4.1.3 Engine cover

The temperature distribution and measure points of the engine cover are shown in Figure 4.2a and the normed temperatures from the measure points are given in Figure 4.5. Here the results from the calculations show good correlation with the test results. There is a slight temperature change along the edge with higher overpredictions in temperature on the right (larger measure point numbers). The same temperature distribution can, quite naturally, be seen in the heat exchangers since hot fluid enters from the right and is gradually cooled down. At earlier stages in the simulation when the heat exchangers were not as properly tuned in, there was a larger change of temperature along the heat exchangers and also along the edge of the engine cover. Hence, it can be expected that the temperature distribution of the heat exchangers influences the temperature of the engine cover notably. Since the heat exchangers are still not perfectly tuned, this might be one explanation of the temperature deviations on the engine cover.

The flow through the heat exchangers and the effect from the cooling fan will also influence the flow over the engine cover. The flow through the heat exchangers is highly restricted with the Porous modeling and the cooling fan does not include any transient effects, but average values. This might not be enough to capture the turbulent behaviour of the flow in this area. Still, the results are close to the tests, so one must doubt if it is worth the extra effort needed to add and run more sophisticated models in this case.

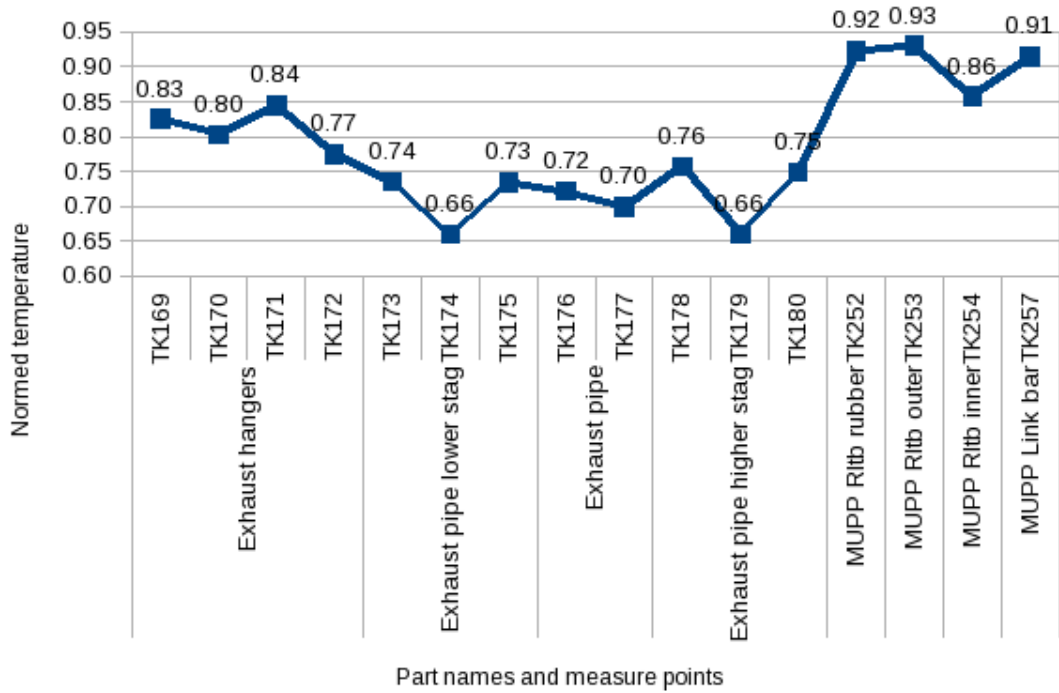


Figure 4.6: Temperatures for the measure points at the exhaust pipe, exhaust pipe stags, exhaust hangers and powertrain mount, normed by their respective measured temperature.

4.1.4 Exhaust pipe and exhaust hangers

The temperature distribution and measure points for the exhaust pipe, exhaust pipe stags and exhaust hangers are shown in Figure 4.2c and 4.2d. The results for the same components, given in Figure 4.6, show underestimated temperatures for the lot. The heat is coming from the exhaust gases into the exhaust pipe and further into the stags and hangers. Since the temperature for the exhaust pipe is low, it is no surprise the temperature is low for the other components.

As explained earlier, catalytic converters of different geometries were used in the calculations and the tests. In the calculations, a second catalytic substrate was present in the catalytic converter. This will give an additional pressure drop with a resulting lower temperature along with possible additional heat being transferred from the exhaust gases in the second substrate. It is hard to guess how much this will affect the flow, but it is also no point in examining other influences until this error source have been eliminated by switching to the correct geometry.

4.1.5 Powertrain Mount

The result for the powertrain mount (MUPP) in Figure 4.2b and 4.6 show quite good correlation with the tests. The components are in direct view of the exhaust system. This means radiation will have a direct impact on the result and the discrepancy in the geometry along with the deviating exhaust gas temperatures might affect

the results. This is a possible reason for the differences from the test results. On the other hand, the results indicate that the dominant effect of radiation from the exhaust system diminish quite rapidly with distance, since these components are a bit further away and the errors in the exhaust system do not affect the results too much.

4.1.6 Cam belt cover, vacuum hose and vacuum tank

The temperature distribution and normed temperature results for the cam belt cover, vacuum hose and vacuum tank are given in Figure 4.7b, 4.7c and 4.8. The results for all these components show good correlation with the test results. The components are different in shape and material, but what they have in common, together with the engine cover, is their placement a bit further away from and with minimal direct view of the exhaust system. This tells us the overall temperature in the engine bay may be well captured, while the volume closer to the exhaust system is not as well captured. It also indicates that while components closer to the exhaust system might need more careful modeling, components further away may very well do with this quite basic modeling and simplified geometries.

4.1.7 Cabin Heater Hose and Turbo Cooling Hoses

The temperature distributions, measure points and normed temperatures of the cabin heater hose and turbo cooling hoses are given in Figures 4.7a, 4.7e, 4.8 and 4.9. The results show overprediction for the cabin heater hose, quite good results for the turbo cooling outlet hose and significant underpredictions for the turbo cooling inlet hose. Despite these different results, what unites these components is the fact that their internal flow dominate the outcome of the result.

The internal boundary conditions in these three components are given as a convective boundary condition with the heat transfer coefficient and ambient temperature specified. These values are given in Table 4.3. The ambient temperatures are normed with the measured temperature for the respective measure point. The results in the table come very close to the results from the simulations, meaning the overall results come close to the specified internal ambient temperatures for the convective boundary condition. An asymptotical value for circular pipe flow with constant surface temperature is used to obtain the heat transfer coefficient [3]. For a constant internal surface temperature, the nusselt number approaches 3.66 for fully developed laminar flow in a circular pipe. From this knowledge an approximate heat transfer coefficient can be calculated from

$$h = \frac{kNu}{D} \quad (4.1)$$

where Nu is the Nusselt number and D the pipe inner diameter.

The validity of both the given constant internal temperature and the heat transfer coefficient must be questioned. The value for the heat transfer coefficient is a crude

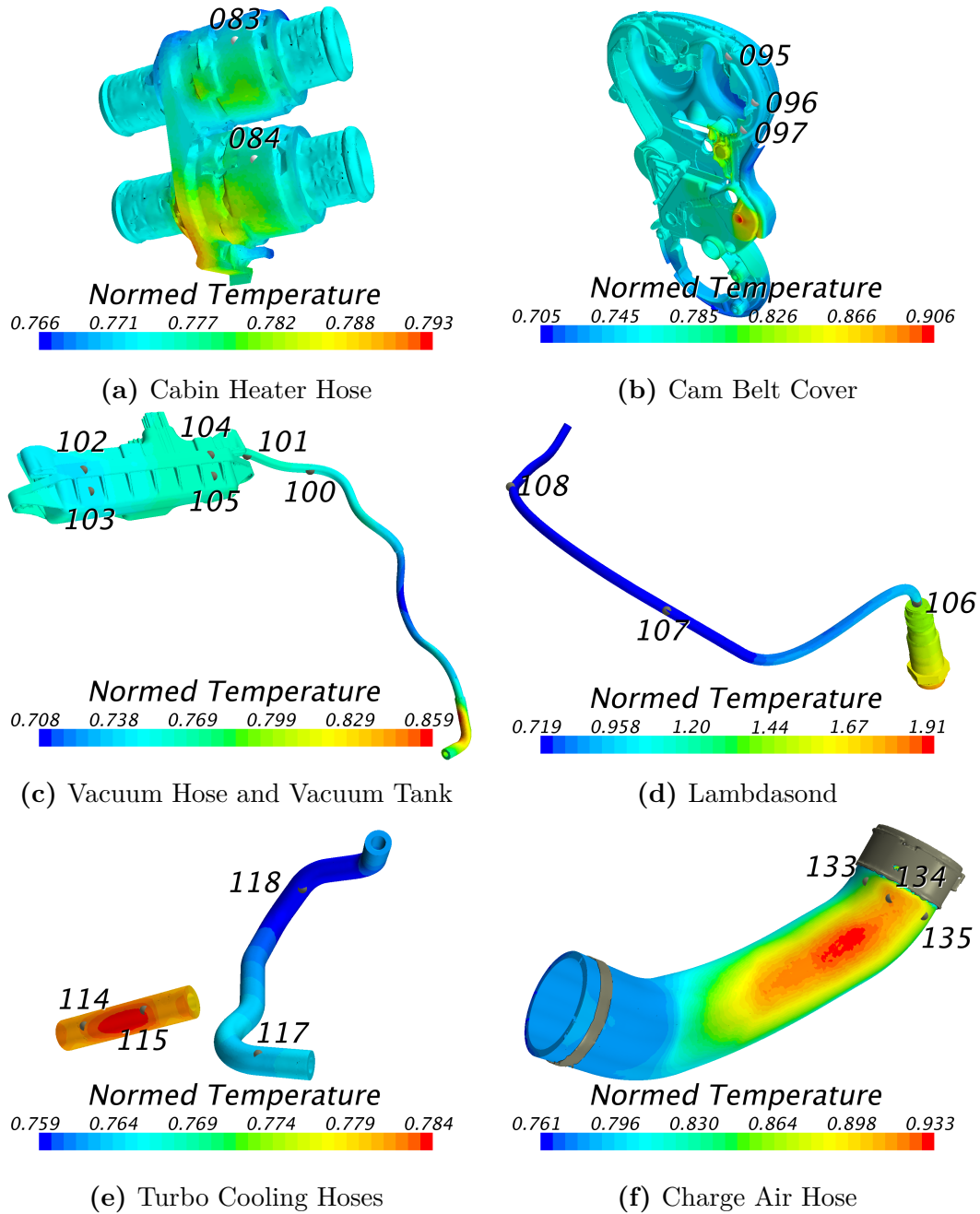


Figure 4.7: Temperature distributions for selected components in the engine bay. Measure point placements are shown in the figures with dots and numbers.

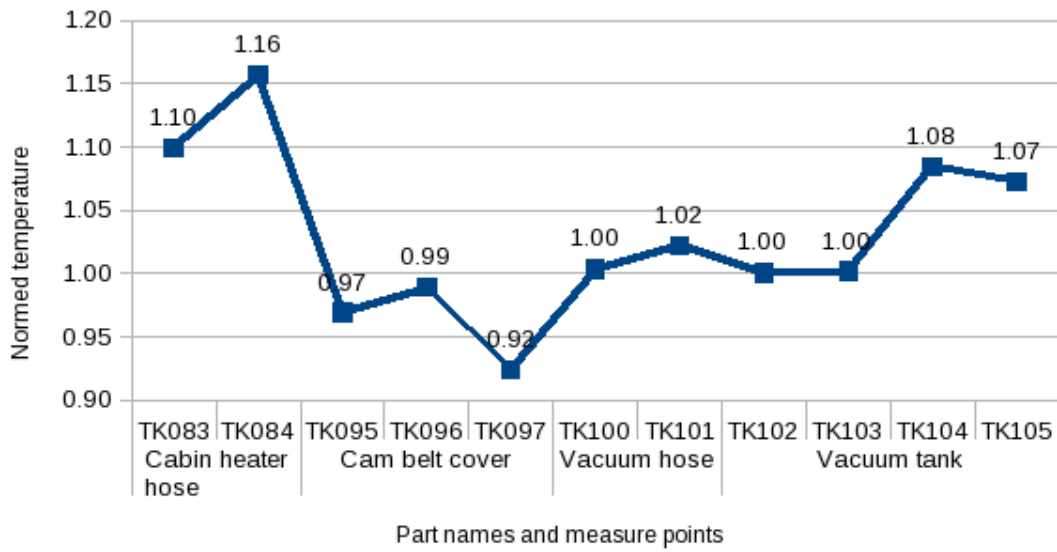


Figure 4.8: Temperatures for the measure points at the cabin heater hose, cam belt cover, vacuum hose and vacuum tank, normed by their respective measured temperature.

Table 4.3: Internal ambient temperatures used for the convective boundary conditions in the cabin heater hose and turbo cooling hoses normed by the measured temperature at the respective measure point along with heat transfer coefficients.

Component	Measure point	Amb. temp	$h [W/m^2K]$
Cabin Heater Hose	TK083	1.08	146
	TK084	1.15	
Turbo Cooling Inlet	TK114	0.65	231
	TK115	0.60	
Turbo Cooling Outlet	TK117	1.00	244
	TK118	1.10	

estimate and the assumption of laminar flow is a mistake since an estimation of the Reynolds number highly exceeds 10000. Moreover, the expected significantly different temperature on the outside of the pipes is likely to have some effect on the temperature on the internal flow rendering it not constant as assumed.

However, since the internal pipe flow was assumed laminar, the used heat transfer coefficients are significantly smaller than what can be expected. This indicates the deviations derive from somewhere else. A reasonable guess is that modeling the components by themselves with adiabatic connections to their surrounding solid components as is done now is not enough. The cabin heater hose has also been modeled as one solid component, while it is actually comprised of several parts. To improve the results for these hoses, a first option should be to prepare the cabin heater hose geometry more carefully and volume mesh also the components adjacent to these hoses.

Table 4.4: Internal static temperatures for the measure points of the charge air hose, normed with their respective temperature measured in the tests.

Measure point	Internal temperature
TK133	0.93
TK134	0.69
TK135	0.63

4.1.8 Charge Air Hose

The temperature distribution, measure points and normed temperatures for the charge air hose is given in Figure 4.7f and 4.9. The internal flow is represented as a static temperature at the internal surface of the hose. This temperature is given in Table 4.4 normed with the corresponding measured temperatures (hence the different values). This temperature is much lower than the measured temperatures, so apparently the internal temperature does not affect the results as much as for the cabin heater hose and turbo cooling hoses. Possibly this larger sized component is less vulnerable being modeled by itself with adiabatic boundaries to adjacent solid parts. The significantly lower thermal conductivity compared to the turbo cooling hoses is also crucial in this difference, but will not explain the different behaviour compared to the cabin heater hose.

The charge air hose is in direct view of, and located close to, several parts of the exhaust system, hence it will be highly affected by radiation. This mean that both the deviating exhaust temperatures, the discrepancies in the geometry and variation in the actual distance to the exhaust system, as discussed in previous sections, will affect the results. Figure 4.7f also show large temperature gradients on the surface of the charge air hose. Due to this, the exact position of the measure point will affect the results too and this may vary slightly between the calculations and tests.

4.1.9 Lambdasond

The results for the lambdasond, given in Figures 4.7d and 4.9, show good correlation for the two measure points further away from the exhaust system. This is in line with the results for the engine cover, vacuum tank and other part not directly prone to radiation. The measure point on the lambdasond closest to the hot catalytic converter is almost 50% too high. Not much conclusions should be drawn from this, since the lambdasond geometry was gravely simplified and no thermal resistance is used in the connection to the catalytic converter. As discussed before, to get viable results from the components closest to the exhaust system, they might need to be modeled with extra care, such as minimal simplifications of the geometry, heat resistances in solid to solid connections and thermal expansion taken into account.

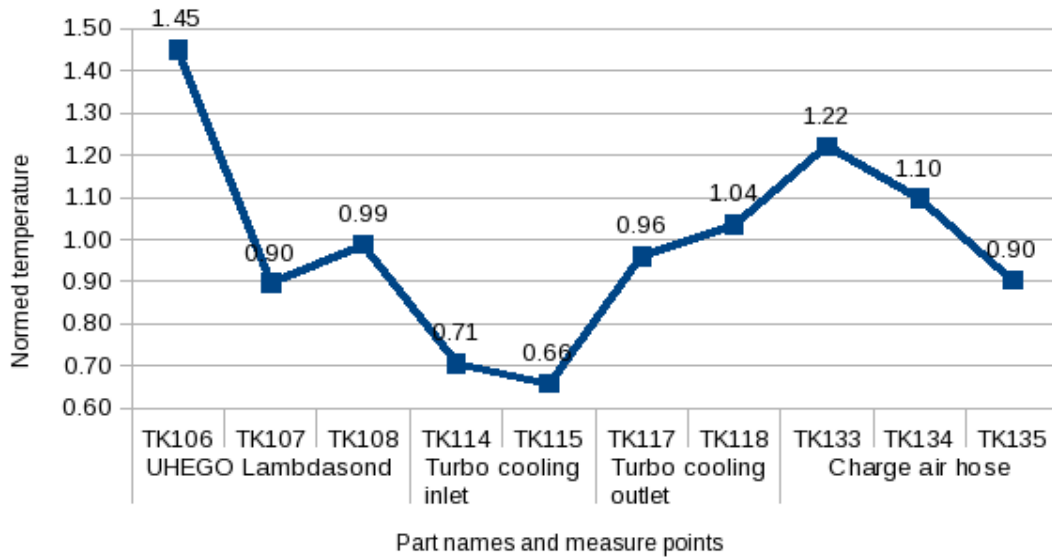


Figure 4.9: Temperatures for the measure points at the lambdasond, turbo cooling inlet hose, turbo cooling outlet hose and charge air hose, normed by their respective measured temperature.

4.2 Interface creation

Quite some effort was made during the model preparation to obtain conformal interfaces between the solid parts and the main fluid domain. This turned out to be too much of a challenge. This is assessed to be an effect of not using the original smooth CAD surfaces but the angular surfaces meshed in ANSA (see 3.1) and not preparing the interfacing surfaces carefully enough.

When CAD surfaces are imported into Star-CCM+, they are divided into triangular surfaces adapted to the geometry of the CAD. More triangles are used to describe highly curved surfaces, while flat surfaces need only a few triangles. The triangles are kept as large as possible while ensuring the curvature is properly maintained. This process is called tessellation. It often results in long, slender triangles, since many surfaces often are curved only in one direction. When executing operations in Star-CCM+ with these tessellated surfaces, there are comparatively few triangles that interact and two surfaces originally in contact are kept in contact since the tessellation maintains the surface curvature quite well. Working with these inputs, boolean subtracts can be performed without damaging the model and imprinting can be performed with perfect contacts as a result.

This is to put in contrast to working with previously meshed surfaces. In a computational mesh it is in general desired to have the triangular surfaces as close to equilateral as possible for calculation purposes. The effect of a meshed CAD surface is that it either need a large number of triangular surfaces to maintain its curvature or that its curvature is defeatured due to number of triangles used. Often, a middle way is chosen. But due to this, the boolean subtract in Star-CCM+ often distort



Figure 4.10: A visualization of the interface at the inside of the Manifold heat shield. Green show interfaced faces, grey are faces not included in the interface.

the parts in use slightly and the imprint does not return perfect contacts since the surfaces are not perfectly in place.

CD-Adapco propose first surface wrapping the parts not to be volume meshed, then imprinting the part to be volume meshed onto the surface wrap creating in-place contacts between them and finally using Extract Volume to obtain the final fluid domain with in-place contacts (later used to create conformal interfaces) automatically created in between the fluid and the other parts. If the original CAD files could have been retrieved, all solid-to-solid contact surfaces on the parts to be volume meshed prepared properly, imported directly into Star-CCM+ and the suggested working order used, a better result with creating the conformal interfaces might have been seen.

Even though conformal interfaces could not be guaranteed in the geometry preparations of this thesis, the obtained interfaces seem to be working properly. Most of the interfaces were not 100% matched, but visualizing the interfaces in Star-CCM+ show very good matches. As an example, a visualization of the interface at the inside of the Manifold heat shield is shown in Figure 4.10. The green indicate interfaced cells, while grey are faces not included in the interface. There are a number of small grey patches, but they are not likely to influence the result. Also, along with the interface visualization, the temperature contour plots show no signs of cold spots or other unphysically large gradients.

To achieve the properly interfaced boundaries, the interface tolerance for most of the solid-fluid interfaces was raised to 0.2 from 0.05. The tolerance is the maximum length a vertex will be moved when trying to interface it and is given as fraction of the smallest boundary face size.

4.3 Calculation stability

As described in Section 3.2.1, very simple calculations were performed to begin with to ensure stability. When stability was confirmed with one setup, more complexity was added and the calculations continued. This was done in several steps and in all of the steps the calculations turned out to be very stable.

During the later stage of the simulation process the A1 coefficient, the Realizability coefficient and Compressibility Correction (all in the $k-\omega$ model solver) was adjusted as advised by CD-Adapco (3.2.2). This to improve the stability even further and give the possibility to raise the underrelaxation factors and achieve faster convergence. No difference in result were observed with these changes and no significant differences in the residuals either. However, no attempts were made to raise the underrelaxation factors to speed up the convergence.

There was no time during the thesis to test a hexahedral mesh or another turbulent solver but similar simulations with hexahedral meshes have been attempted at Volvo Car Corporation with stability issues present. The polyhedral mesh and SST $k-\omega$ solver is both said to give stability to the calculations and this is confirmed by the simulations in this thesis.

4.3.1 Residual fluctuations

When the solution is converged, there are still residual fluctuations present in the temperature and velocity. Also, the y- and z-momentum residuals (transversal to the main flow direction) have not dropped lower than about 0.002. This behaviour much resembles vortex shedding, where vortices detach periodically from different directions on the backside of an object. With a steady state solver, this phenomena can not be properly captured, but numerical instability is known to cause a similar behaviour. That is, a vortex shedding induced by numerical instability instead of transient flow behaviour.

Especially with a $k-\omega$ model, this problem could be expected, since it is known to produce unphysical separations. The suggested adjustment of the SST $k-\omega$ A1 coefficient could provide a possible reduction of the symptoms, but in this case no significant improvements was observed. The problem could also possibly be adressed with an improved resolution of the mesh to more thoroughly resolve the boundary layers. However, with this complex geometry, it is unlikely that the problem can be fully cured.

The most reasonable way to treat the issue would be to use mean values of the variables to achieve acceptable steady state results. This is what was done in this case. About 400 iterations were needed for the mean temperature values to stabilize.

4.4 Future work

This thesis may be viewed upon as an elaborate starting point for these kinds of complex complete system analyses. As a lot of time was consumed by the geometry preparation and meshing phases, there was not enough time to look into many different aspects of the calculations and no time to widen the scope of the investigations. This will be left for the future and some suggestions will be presented below.

4.4.1 Polyhedral vs. hexahedral mesh

For the calculations in this thesis mainly polyhedral cells was used in the meshes. As mentioned, similar simulations have been attempted at Volvo with hexahedral cells with some stability issues occurring. No proper comparison have been made though and a full comparison between the two approaches is in order. The polyhedral cells are known to take significantly longer computational time to be meshed but on the other hand the mesh is said to give more stability and faster convergence (equal lower computational time). The results may also be more accurate. The question is how the complete process of meshing and simulating is affected. Can the expensive meshing of the polyhedral cells be motivated by the savings in the simulation times and more accurate results or is the hexahedral mesh still a more viable option?

4.4.2 Deeper study of the manifold heat shield

The manifold heat shield was anticipated difficult to capture properly within the calculations and the results did not reach a satisfying level in this thesis. To begin with, a comparison of temperatures at the outer surface of the exhaust manifold should be performed to verify that the flow of the internal exhaust gases are properly captured and the heat transfer through the solid walls is ok. If this can be confirmed, a next step could be to include thermal expansion of the exhaust manifold in the calculations to investigate how it affects the results and if it is possible to achieve better correlation of the data with this taken into account.

4.4.3 Correction of geometrical flaws

Part of the deviations in temperature can be connected to faulty geometry or too severe simplifications of the geometry. This includes especially the faulty geometry of the catalytic converter, the cabin heater hose being surface wrapped and the geometry of the lambda sond being simplified a lot. Also, the cabin heat hose, the turbo cooling hoses and the charge air hose were treated as isolated solid components with adiabatic boundaries to all their adjacent solids. Taking the time to prepare these geometries more thorough and including their adjacent solids in the simulations would most likely give a better view of the thermal balance in the vicinity of the exhaust system.

4.4.4 Transient load cases

One of the most difficult situations a car must be able to handle is thermal soak (when the engine is stopped after being used at high loads). The cooling will be driven from natural convection and possibly the cooling fan. To be able to properly predict thermal soak (and other important transient load cases) could make a lot of the time consuming tests performed today superfluous. If the improvements suggested above result in temperatures correlating within a few percent margin with the test results, a natural step would be to investigate the possibility of performing transient flow simulations like the thermal soak. This would likely require more components of the engine to be volume meshed and included in the simulation to account for the thermal energy being accumulated in the engine during run.

Bibliography

- [1] Horst Bauer. *Automotive Handbook*. Robert Bosch GmbH, Postfach 30 02 20, D-70442 Stuttgart, 4th edition edition, 1996.
- [2] Jacob Bear. *Dynamics of fluids in porous media*. Dover books on physics and chemistry. Dover, New York, 1988. 87034940 Jacob Bear. ill. ; 23 cm. "An unabridged, corrected republication of the work first published by the American Elsevier Publishing Company, Inc., New York, 1972, in its Environmental Science series"—T.p. verso. Bibliography: p. 733-756. Includes index.
- [3] Yunus A. Çengel and Afshin J. Ghajar. *Heat and mass transfer : fundamentals & applications*. McGraw-Hill, New York, 4th edition, 2011. 2009051322 GBA9A5670 Yunus A. Çengel, Afshin J. Ghajar. ill. ; 27 cm. + 1 DVD-ROM (4 3/4 in.) Includes bibliographical references and index.
- [4] CD-Adapco. *STAR-CCM+ User guide. Version 9.06*, 2015.
- [5] Lars Davidson. Numerical methods for turbulent flow. Available at http://www.tfd.chalmers.se/~lada/comp_fluid_dynamics/postscript_files/chapter_5.pdf (2015/09/30), January 2005.
- [6] Lars Davidson. Fluid mechanics, turbulent flow and turbulence modeling. Available at http://www.tfd.chalmers.se/~lada/postscript_files/solids-and-fluids_turbulent-flow_turbulence-modelling.pdf (2015/09/30), June 2015.
- [7] Magnus Ekh and S. Toll. Mechanics of solids & mechanics of fluids. introduction to continuum mechanics. Available at <http://www.tfd.chalmers.se/~lada/MoF/postscript/SF-I.pdf> (2015/09/30), August 2014.
- [8] Symscape Computational Fluid Dynamics Software for All. Polyhedral, tetrahedral, and hexahedral mesh comparison. Available at <http://www.symscape.com/polyhedral-tetrahedral-hexahedral-mesh-comparison> (2015/09/30), February 2013.
- [9] John R. Howell, Robert Siegel, and M. Pinar Mengüç. *Thermal radiation heat transfer*. CRC, Boca Raton, Fla., 5th ed. / john r. howell, robert siegel, m. pinar mengüç. edition, 2011. GBB065497 bnb Formerly CIP. Uk Siegel's name appears first on the earlier edition. Includes bibliographical references and index.

- [10] F.R. Menter. Two-equation eddy-viscosity turbulence models for engineering applications. *AIAA Journal*, 32(8), August 1994.
- [11] F.R. Menter, M. Kuntz, and R. Langtry. Ten years of industrial experience with the sst turbulence model. *Bergell House, Inc*, 2003. K. Hanjalić, Y. Nagano and M. Trummers (Editors).
- [12] Milovan Peric and Stephen Ferguson. The advantage of polyhedral meshes. Available at http://www.plmmarketplace.com/upload/Temp/The_Advantage_of_polyhedral_1.pdf (2015/09/30), 2004.
- [13] H. K. Versteeg and W. Malalasekera. *An introduction to computational fluid dynamics : the finite volume method*. Prentice Hall, Harlow, 2nd ed. edition, 2007. GBA649081 bnb H.K. Versteeg and W. Malalasekera. Formerly CIP. Uk Includes bibliographical references (p. [472]-494) and index.
- [14] David C. Wilcox. Reassessment of the scale-determining equation for advanced turbulence models. *AIAA Journal*, 26(11), November 1988.
- [15] David C. Wilcox. *Turbulence Modeling for CFD*. DCW Industries, Inc., 5354 Palm Drive, La Cañada, California 91011, 1st edition, November 1994.